

REU 2017

BEIJING



Research Experience for Undergraduates

Section 3

Support for the REU program is provided by the NSF MRSEC program (DMR-1120296) and the REU Site program (DMR-1460428).

TABLE OF CONTENTS

REU	Faculty Advisor	Page
Ramirez, Maria	Prof. Greg Fuchs	03
Shankel, Shelby	Prof. Brett Fors	10
Slyker, Leigh	Prof. Lawrence Bonassar	15
Timmins, Sarah	Prof. Christopher Ober	19
Tirado, Erika	Prof. Robert DiStasio Jr.	24
Tobar, Celeste	Prof. Song Lin	30
Allen, Anthony	Prof. Song Lin	36
Alqahtani, Omar	Prof. Hector Abruña	45

A Computational Two-Temperature Model of Picosecond Laser Heating and Diffusion at Low Temperatures

Maria Ramirez¹, Isaiah Gray², Gregory Fuchs²

¹Department of Physics, Fullerton College, Fullerton, CA 92832

²Department of Applied and Engineering Physics, Cornell University, Ithaca, NY 14853

Abstract— A novel type of magneto-thermal microscope has been developed, based on thermal gradients generated by a focused pulsed laser. This microscope is currently capable of imaging magnetic dynamics at room temperature with submicron spatial resolution and picosecond temporal resolution. However, many interesting magnetic phenomena are only observable at low temperature, below 20 K. Hence, we seek to expand the microscope's capability down to 4 K. Laser heating and diffusion is more complicated at low temperature than at room temperature, as the electron-phonon scattering time becomes comparable to the laser pulse width. This study simulates laser-heated temperature profiles in magnetic thin films at low temperatures to gain a quantitative understanding of the spatial and temporal resolution of magneto-thermal microscopy at low-temperatures.

I. Introduction

Magnetism has many applications in technology including in sensors, data storage in hard drives and MRAM (magneto-resistive RAM). Additionally, it has many interesting applications in research, such as in spintronics. Advances in spintronics, have

demonstrated that when a current of electrons with spin up and spin down induces a current of spin, a torque is created, that can switch the direction of magnetization of a material¹. Recent work has demonstrated that magnetism can be controlled on the nanoscale without a magnetic field by exploiting this spin-orbit effect to switch magnetic devices with electrical current. This work is scientifically interesting and has direct application in magnetic storage and MRAM^{2,3}. It is therefore vital to image nanoscale dynamics in magnetic devices.

We have previously developed a new kind of time-resolved magnetic microscope based on heat transfer⁴. Our microscopy technique uses the time-resolved anomalous Nernst effect (TRANE), shown in figure 1, in which a focused thermal gradient normal to the magnetic moment of the material induces an in-plane local electric field that is perpendicular to both the magnetic moment and thermal gradient.

$$E_{ANE}(x, t) = -NVT(x, t) \times \mu_0 M(x, t) \quad (1)$$

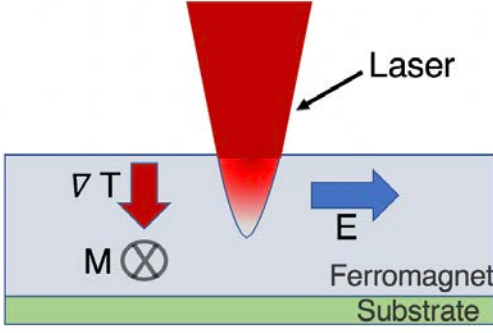


Figure 1. Diagram of the anomalous Nernst effect

The resulting voltage is then measured and used to image the magnetization direction. Using this microscopy technique, it is possible to image nanoscale magnetic dynamics, on the picosecond time scales at which they typically occur⁴.

Magnetic microscopy is fundamental to new discoveries in magnetism. The ability to image nanoscale magnetic dynamics such as antiferromagnetism and chiral magnetism, however, is best studied at low temperatures. Because our microscope uses a laser to generate heat, it is important that we understand how laser heating and heat diffusion in multilayer magnetic devices works at low temperatures.

At room temperature, with a picosecond laser, we can use a one-temperature model to describe heating of the metal since the electron-phonon scattering time is fast compared to the laser pulse duration, in the order of femtoseconds⁵.

$$\rho C_p \frac{\partial T}{\partial t} = \nabla \cdot (K \nabla T) + S(t) \quad (2)$$

Here, ρ is the mass density, C_p is the specific heat, and K is the thermal conductivity. $S(t)$ is the heat source, given as

$$S(t) = (1 - R)I\alpha e^{-\alpha|z|} e^{-\frac{x^2}{2\sigma^2}} \quad (3)$$

Here, R is the reflectivity coefficient, I is the laser intensity, α is the absorption coefficient, and σ is the pulse radius. However, the electron-phonon scattering time is temperature dependent. As we lower the external temperature the scattering time also decreases. Once we reach temperatures below 20 K, the electron-phonon scattering time is in the order of picoseconds and becomes comparable to the laser pulse duration. Thus, the one-temperature model can no longer be used to accurately describe thermal diffusion. Instead, we use a two-temperature model of laser heating with two equations to describe heating of the electrons and phonons⁵:

$$C_e(T_e) \frac{\partial T_e}{\partial t} = \nabla \cdot (K \nabla T_e) - G(T_e - T_l) + S(t), \quad (4)$$

$$C_l \frac{\partial T_l}{\partial t} = G(T_e - T_l), \quad (5)$$

where C_e is the electron heat capacity, C_l is the lattice heat capacity, K is the thermal conductivity, and G is the electron-lattice coupling factor. This model neglects the thermal conductivity of the lattice, which is acceptable for a metal. However, when using an insulating substrate, the thermal conductivity of the lattice needs to be taken into account.

Various modeling and experiments dealing with the two-temperature model exist^{5,6,7}, but nearly all of them use a femtosecond laser at room temperature. Therefore, this work is intended to develop a two-temperature model of laser heating and diffusion using a picosecond laser at low temperature.

II. Materials and Methods

A finite element simulation program, COMSOL, was used to simulate laser heating in a 20 μm long, 5 μm wide and 1 μm thick film of iron (figure 2). To solve (1), (4) and (5), COMSOL divides the

problem into many small finite elements and finds solutions for these elements. It then recombines the various elements to give an approximate final solution, using boundary conditions and initial conditions to impose extra restrictions on the solution⁹.

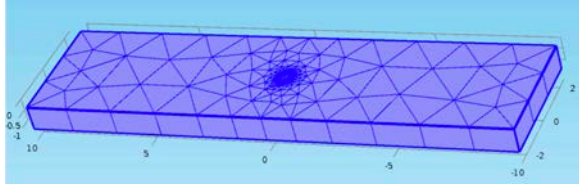


Figure 2. Geometry of 20 μm long, 5 μm wide and 1 μm thick film of iron with triangular meshing from COMSOL.

We first simulated laser heating using the prepackaged heat transfer module from COMSOL and used it as a point of reference for the other simulations. The simulation was modeled as a 3D problem using a time-dependent solver, and the following parameters:

Physical Constants of Iron	
Electron-Phonon Coupling Factor	$4.34 \times 10^{16} \text{ W/m}^3 \text{ K}$
Absorption Coefficient	$2.49 \times 10^8 \text{ 1/m}$
Thermal Conductivity	$76.2 \text{ W/m} \cdot \text{K}$
Lattice Heat Capacity	$3.52 \times 10^6 \text{ J/m}^3 \text{ K}$
Electron Heat Capacity	$2.48 \times 10^4 \text{ J/m}^3 \text{ K}$

Table 1. These are the parameter constants used in the simulation

A 3 ps laser with a fluence of 1 mJ/cm^2 was used. The laser heat source (3) is assumed to have a Gaussian spatial distribution with a radius of 0.375 μm . The initial temperature was set to 293.15 K. We

also set a zero-flux boundary condition on all outer boundaries except the top surface. The simulation was run at room temperature 293.15 K for 1 ns with time steps of 10 ps and time steps of 0.5 ps for 10 ps.

We then simulated laser heating using the one-temperature model in COMSOL via the custom PDE module. The simulation was modeled as a 2D axisymmetric problem using the parameters found in Table 1. The heat source is given by equation (3). Both the electron and lattice temperatures were initially set to 293.15 K and flux was set to zero at all outer boundaries except the top surface.

A third simulation of the two-temperature model was also implemented in COMSOL using the coupled custom PDE module. The simulation was modeled as a 2D axisymmetric problem using a time dependent solver and with the parameters found in table 1. The initial lattice and electron temperatures were both set to 293.15 K and a zero-flux boundary condition was imposed on all outer boundaries except the top surface

III. Results and Discussion

Both the one-temperature model and the model using the prepackaged heat transfer in solids module showed a temperature increase lasting a few picoseconds, followed by a slower decay. The z component of the thermal gradient followed a similar trend of a rapid rise in the thermal gradient followed by a slower decay, in both the one-temperature and the heat transfer in solids model. The thermal gradient in both models decayed quicker than the temperature. We measure ∇T_z , in particular, because in principle it is the only term we are sensitive to in the microscope. We measure the voltage in the x direction which is only due to the thermal gradient in the z direction.

The two-temperature model showed a rapid increase in both the lattice temperature and z component of the thermal gradient, followed by a slow decay. Although, the thermal gradient decayed at a faster rate than the temperature. The electron temperature exhibited a high increase that lasted around 3 ps. The z-component of the electron temperature gradient also showed a short-lived increase that lasted about 2 ps.

Although, all three models showed similar trends in the temperature and thermal gradient, they did not match quantitatively. The model using the heat transfer in solids module (figure 3) showed a maximum temperature increase of about 50 K and had a relaxation time close to 30 ps, while the one-temperature model (figure 5) showed a maximum temperature increase of 40 K and a longer decay time of about 70 ps. The two-temperature model showed a smaller maximum increase in the lattice temperature (figure 7) of about 17 K and a decay time of 700 ps, which is one order of magnitude slower than the other two models. The two-temperature model also showed an 601 K maximum increase of the electron temperature that lasted approximately 3 ps (figure 8).

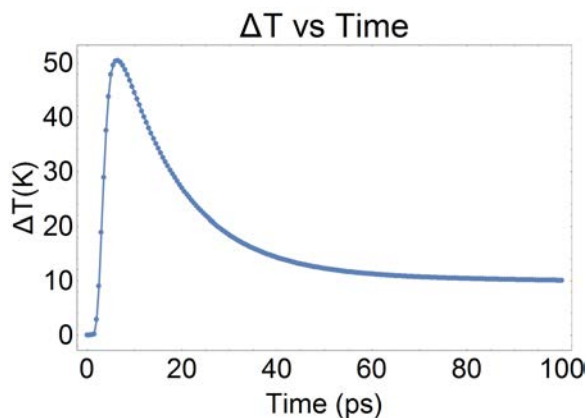


Figure 3. Change in temperature at the center, through the thickness, of a 30 nm thick iron film heated by a 3 ps laser with a 1 mJ/cm^2 fluence using the heat transfer in solids module at $T= 293.15 \text{ K}$.

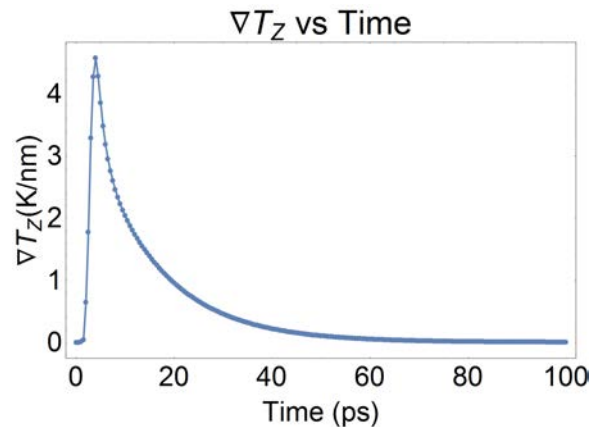


Figure 4. Z-component of thermal gradient at the center, through the thickness, of a 30 nm thick iron film heated by a 3 ps laser with a 1 mJ/cm^2 fluence using the heat transfer in solids module at $T= 293.15 \text{ K}$.

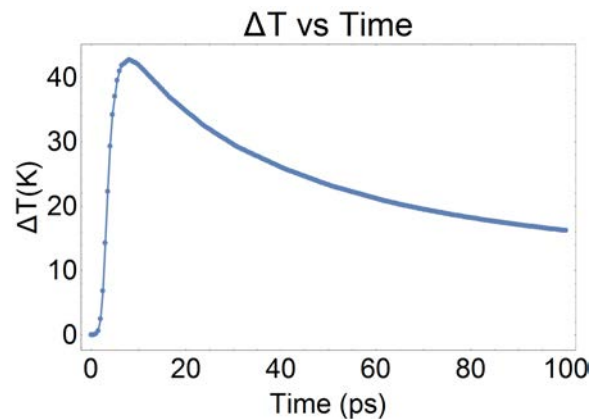


Figure 5. Change in temperature at the center, through the thickness, of a 30 nm thick iron film heated by a 3 ps laser with a 1 mJ/cm^2 fluence using a one-temperature model at $T= 293.15 \text{ K}$.

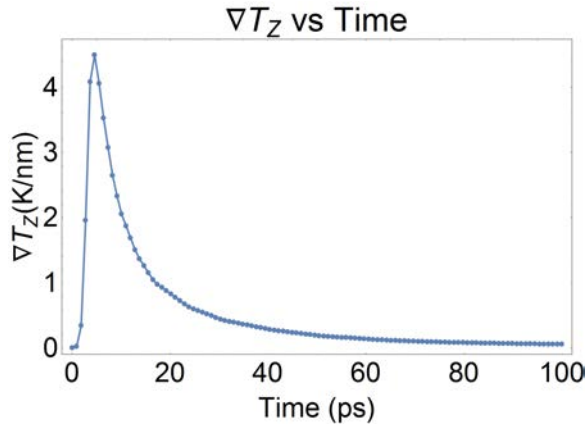


Figure 6. Z component of thermal gradient at the center, through the thickness, of a 30 nm thick iron film heated by a 3 ps laser with a 1 mJ/cm^2 fluence using the one-temperature model, starting at $T= 293.15 \text{ K}$.

The one-temperature and heat transfer in solids models showed similar increases in the z-component of the temperature gradient of 4.49 K/nm and 4.58 K/nm , respectively (figures 4 and 6). They also had matching decay times of about 15ps each.

The two-temperature model, however, did not exhibit the same increase in temperature gradient as the other two models. The z-component of the electron temperature gradient reached a maximum of 9.7 K/nm and lasted for about 2 ps (figure 10), while the z-component of the lattice temperature gradient had an amplitude of 0.23 K/nm (figure 9) and decayed in about 150 ps.

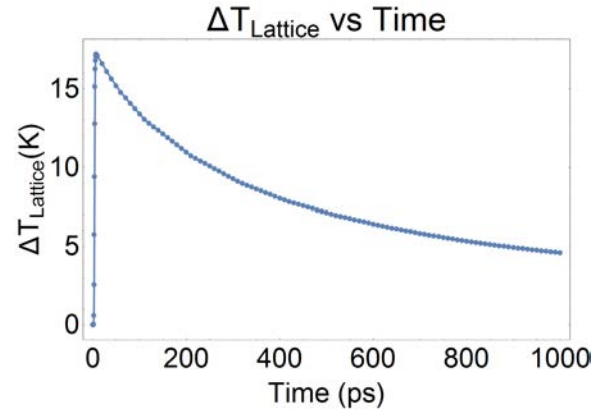


Figure 7. Change in lattice temperature at the center, through the thickness, of a 30 nm thick iron film heated by a 3 ps laser with a 1 mJ/cm^2 fluence using the two-temperature model, starting at $T= 293.15 \text{ K}$.

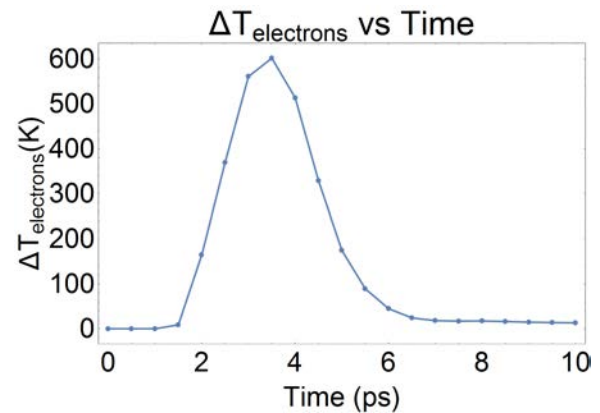


Figure 8. Change in electron temperature at the center, through the thickness, of a 30 nm thick iron film heated by a 3 ps laser with a 1 mJ/cm^2 fluence using the two-temperature model, starting at $T= 293.15 \text{ K}$.

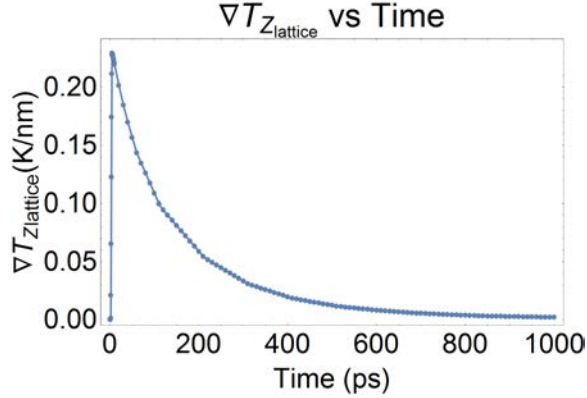


Figure 9. Z component of lattice thermal gradient at the center, through the thickness, of a 30 nm thick iron film heated by a 3 ps laser with a 1 mJ/cm^2 fluence using the two-temperature model, starting at $T=293.15 \text{ K}$.

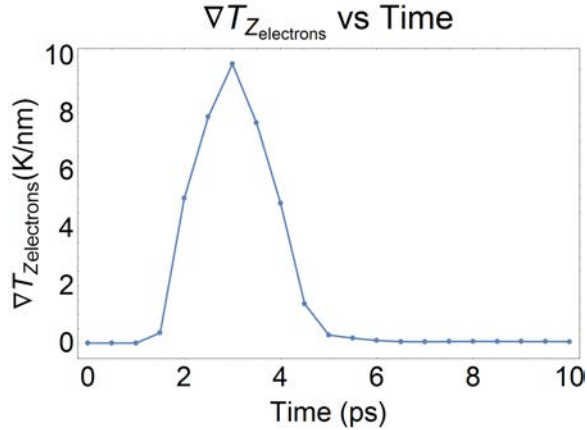


Figure 10. Z component of electron thermal gradient at the center, through the thickness, of a 30 nm thick iron film heated by a 3 ps laser with a 1 mJ/cm^2 fluence using the two-temperature model, starting at $T=293.15 \text{ K}$.

IV. Conclusion

Three models of laser heating and diffusion were presented in this paper, one using the COMSOL heat transfer in solids package and the other two using custom PDEs. It is expected that these three models give similar results at room temperature, however, that was not the case. Although they qualitatively match, quantitatively, all three predict different decay times and have

differing amplitudes. Further work must be done on the implementation of the two-temperature and one-temperature models to determine what exactly is causing the models to give unexpected results. By performing validity checks with similar simulations done by other groups, we hope to be able to narrow down the possible problems with the simulations. Furthermore, it is possible that this model cannot be implemented in the custom PDE using the coefficient PDE, and instead requires an implementation using the weak form PDE from COMSOL.

V. Acknowledgements

I would like to thank Professor Greg Fuchs for welcoming me into his group, and Isaiah Gray for his mentorship and guidance throughout the summer. This work was supported by the Cornell Center for Materials Research with funding from the NSF MRSEC program (DMR-1120296) and the REU Site program (DMR-1063059).

References

- [1] A. R. Mellnik, et al., Spin Transfer Torque Generated by a Topological Insulator, *Nature* 511, 449–451, (2014)
- [2] Behin-Aein, Behtash, et al. “Proposal for an All-Spin Logic Device with Built-in Memory.” *Nature Nanotechnology* 5, 266–270 (2010)
- [3] Cubukcu, Murat, et al., Spin-orbit torque magnetization switching of a three-terminal perpendicular magnetic tunnel junction, *Appl. Phys. Lett.* 104, 042406 (2014); doi: 10.1063/1.4863407
- [4] J.M. Bartell, D. H. Ngai, Z. Leng, and G.

D. Fuchs. Toward a table-top microscope for nanoscale magnetic imaging using picosecond thermal gradients. *Nat. Commun.* 6, 8460 (2015).

[5] Qiu, T. Q., and Tien, C. L., Heat Transfer Mechanisms During Short-Pulse Laser Heating of Metals, *Journal of Heat Transfer* 115, 835-837 (1993)

[6] Qiu, T. Q., Tien, C. L., Femtosecond laser heating of multi-layer metals - I Analysis, *International Journal of Heat and Mass Transfer* 37, 2789-2797 (1994)

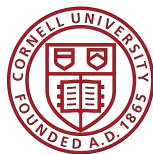
[7] Chen, J. K., et al, A semiclassical two-temperature model for ultrafast laser heating, *International Journal of Heat and Mass Transfer* 49, 307–316 (2006)

[8] Shen, Minghao (2005). Low Temperature Electron-Phonon Interaction in Disordered Metal Thin Films and Applications to Fast, Sensitive Sub-Millimeter Photon Sources and Detectors. (PhD dissertation), Yale University

[9] “FEA Software Definition with Simulation Examples.” COMSOL, www.comsol.com/multiphysics/fea-software.

[9] Kittel, C., 1967, *Introduction to Solid State Physics*, John Wiley, New York, NY.

[10] Ashcroft, N.W., Mermin, N.D., 1976, *Solid State Physics*, Saunders College, Philadelphia, PA.



Formation of Graft Polymers Through Photocontrolled Cationic and Radical Polymerizations

Shelby L. Shankel, Veronika Kottisch, and Brett P. Fors

ABSTRACT: Graft copolymers are found in many materials, from plastics for the packaging of food in the supermarket to biocompatible membranes for plasma separation. With a multitude of applications, there are many ways to make graft polymers, but there is still an effort to find more facile and green methods for doing so. This paper investigates a potential method for synthesizing graft polymers in one pot by using different wavelengths of visible light to selectively polymerize the backbone with a cationic mechanism and the branches utilizing radical polymerization. The findings show that the backbone and branches can successfully be formed if the reagents are added stepwise. However, more optimization is currently needed in order to adapt these conditions to a one pot system.

Goal This research endeavors to form graft polymers in one pot using visible light to interconvert between cationic and radical polymerization.

Introduction Graft polymers have many applications in materials ranging from those used to make everyday items to those used in emerging technologies. The ability for graft polymers to make high impact materials is utilized for packaging, such as CD covers, plastic egg cartons, and trays for meat and vegetables. These high impact materials are also employed in the casing and linings of electronics and appliances, as well as in biology for plastics used in items such as petri dishes.^{1,2} Within the biomedical field, graft copolymers can also be used for biocompatible membranes. Artificial skin can be made from films of graft copolymers, with the potential to avoid bacterial infections, increase water permeability, and adhere to skin with painless removal.³ Graft polymers can also be utilized in plasma separation, drug delivery, and gene therapy.^{4,5} More recently, graft copolymers have been used to create solvent-free super soft elastomers.^{6,7} The branches in the densely grafted copolymers act as solvent to give the material super soft properties, which is beneficial in applications where softness is necessary but solvent can create issues, such as in medicine and electronics. Graft polymers may also reflect visible light, which could have potential applications in photonics.⁸

With an abundance of current and potential applications for graft copolymers, it is essential to have easy and green syn-

theses available. Therefore, this work looks into a one pot method that uses different wavelengths of visible light to selectively polymerize the backbone and branches of graft polymers. In this way, the synthesis can be done in one vial that only requires a change in wavelength to make the graft copolymers. By using visible light, this process also takes advantage of a benign and noninvasive energy source with the capability of spatial and temporal control.

This project is based off of work recently done in the Fors group, which uses green and blue sources to initiate cationic and radical polymerization respectively from the same initiator (Figure 1).⁹ In the cationic polymerization, isobutyl vinyl ether (IBVE) is selected, whereas methyl acrylate (MA) is radically polymerized. The ability to selectively choose between the types of polymerizations is a result of the absorption of the photocatalysts used in the reactions: 2,4,6-tris(*p*-methoxyphenyl)pyrylium tetrafluoroborate (TMPP) and Ir(ppy)₃. As shown in the absorption spectra in figure 2, only the pyrylium catalyst absorbs green light, but both photocatalysts absorb blue light. Therefore, in one pot reactions, only TMPP can initiate cationic polymerization at the wavelength of the green LEDs, allowing for the selective polymerization of IBVE (Figure 3a). However, both catalysts absorb blue light, and therefore, both can initiate polymerization at this wavelength (Figure 3b, c). The ability to choose between which polymerizations are initiated allows for selectivity over the structure of the linear polymers formed.

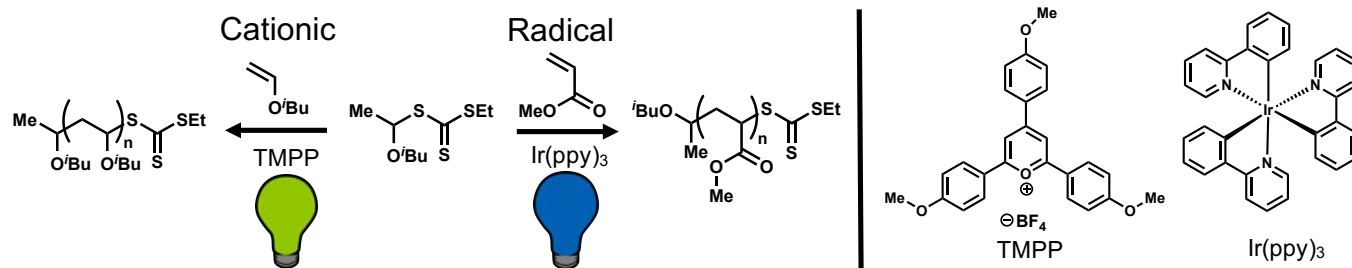


Figure 1. Cationic and radical polymerization are initiated from the same initiator using different photocatalysts and light.

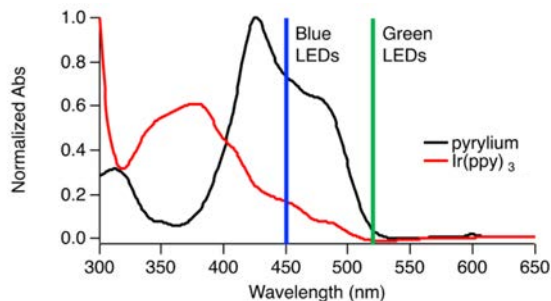


Figure 2. The absorption spectra of the photocatalysts show that only the pyrylium catalyst can absorb green light, giving the system selectivity.⁹

This work attempts to expand this concept of using different wavelengths of visible light to selectively polymerize different types of monomers to make complex polymer architectures in one pot. In the proposed synthesis, the branching monomer (BM) shown in figure 4 is used. The vinyl ether subunit allows the branching monomer to be copolymerized with IBVE via a cationic mechanism to form the backbone of the graft polymer by using green light. The end of the monomer features a trithiocarbonate end group as an initiator, allowing MA to radically polymerize off of the backbone to create branches under blue light (Figure 4). Therefore, by using the selectivity of the two visible light sources, graft copolymers can be made in one pot.

Procedure

Polymerizations

All polymerizations were set up in a Unilab MBraun glove box with nitrogen atmosphere. The vials were equipped with stir bars and septum caps. Any reagents that needed to be weighed out were added first. Then, solutions were added in the following order: initiator, monomer, photocatalysts, and internal standard. Stock solutions of the initiator and various photocatalysts were prepared in DCM. Once sealed, the vials were removed from the glove box and placed in crystallization dishes using blue diode led® BLAZE™ lights (450 nm, 2.88 W/ft) or green LED strip lights (FlexTec®, 520 nm, 4.5W/ft). The reactions were cooled by blowing compressed air over the reaction vial.

Analysis of Polymers

The polymer samples were analyzed by proton nuclear magnetic resonance (¹H-NMR) in deuterated chloroform

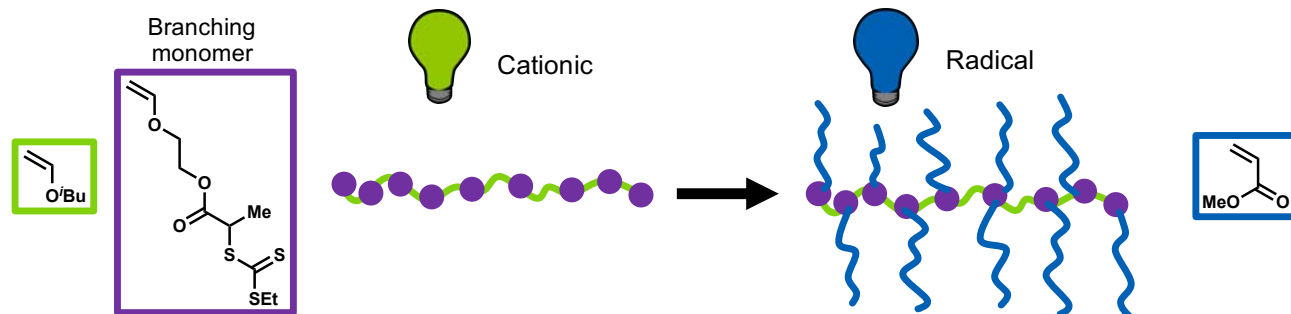


Figure 4. Schematic of the proposed route for the one pot formation of graft polymers using green and blue light.

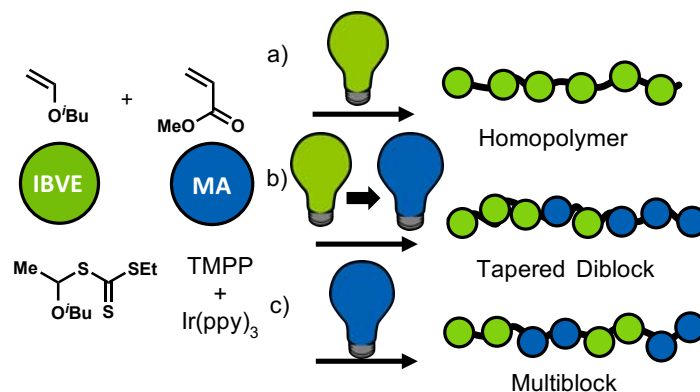


Figure 3. Selectivity in the structure of linear polymers by interconverting between green and blue light to switch from cationic to radical polymerization, respectively.

and gel permeation chromatography (GPC) in tetrahydrofuran. The theoretical number average molecular weight ($M_{n,theo}$) is calculated from ¹H-NMR conversion, while the experimental number average molecular weight ($M_{n,exp}$) is obtained from GPC.

Synthesis of Branching Monomer

A 250 mL round bottom flask and stir bar were flame dried and charged with nitrogen. At 0 °C, dry dichloromethane (50 mL), triethylamine (10.5 mL, 1.5 eq, 75 mmol), and ethylene glycol vinyl ether (5.4 mL, 1.2 eq, 60 mmol) were added through the septum. 2-bromopropionyl bromide (5.2 mL, 1 eq, 50 mmol) was added dropwise over a span of 20 minutes. After an additional 10 minutes, the flask was removed from the ice bath and warmed to room temperature. The reaction was allowed to sit overnight and quenched with water. The water layer was separated and washed with DCM twice. The combined organic layers were washed with brine, dried with magnesium sulfate, filtered, and concentrated in vacuo. Flash column chromatography was run in 4:1 hexane/EtOAc, followed by DCM.

A three armed round bottom flask equipped with a stir bar was flame dried and backfilled with nitrogen. NaH with 60% dispersion in mineral oil (1.12 g, 1 eq, 28 mmol) was placed into the flask and washed three times with ~5 mL hexanes under constant nitrogen flow. 10 mL of dry ether were added. At 0 °C, ethanethiol (2.1 mL, 1 eq, 28 mmol) was added dropwise to the flask over 10 minutes. Pressure was occasionally released with a needle due to the evolution of hydrogen gas. Once the addition was done, the flask was allowed to warm to room temperature and react for 10 minutes. The flask was placed in an ice bath again, and carbon disulfide (1.9 mL, 1.1 eq, 30.8 mmol) was added

dropwise over 10 minutes to yield a yellow cloudy solution. With the addition done, the flask was warmed to room temperature and allowed to react. After 2 hours, the reaction flask was cooled to 0 °C again. The product from the previous step was placed under a nitrogen atmosphere, dissolved in dry ether, and cooled in the ice bath. This solution was then added to the reaction flask dropwise over 20 minutes. After the addition, the flask was warmed to room temperature. The reaction was monitored by TLC. At full conversion, the reaction was quenched with saturated aqueous sodium bicarbonate solution. The aqueous layer was washed twice with ether. The combined organic layer was extracted with water and brine, dried with sodium sulfate, and concentrated in vacuo. Flash column chromatography with 5% EtOAc in hexanes was used to purify the product.

Results/Discussion To prove that this was a viable route for synthesizing graft polymers, the backbone and the branches were first synthesized separately. For the backbone, the branching monomer and IBVE were placed under

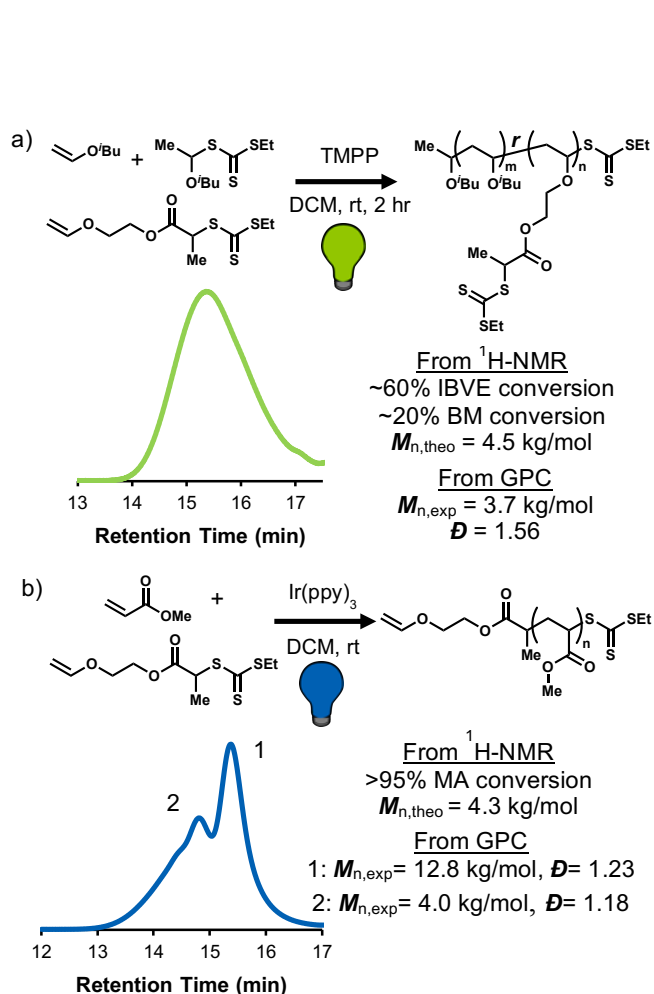


Figure 5. a) Cationic copolymerization of IBVE and BM under green light. b) Radical polymerization of MA initiated by the BM under blue light.

green light with the initiator and TMPP, as shown in figure 5a. From the data, $M_{n,theo}$ was consistent with $M_{n,exp}$ and the dispersity was narrow enough to demonstrate control over the length of the polymer chains. Therefore, the branching monomer successfully copolymerized with IBVE through a cationic mechanism using green light. As the next proof of concept, the branching monomer acted as the initiator for the radical polymerization of MA with Ir(ppy)₃ as the photocatalyst under blue light. From ¹H-NMR, the theoretical molecular weight matched that of the peak labelled 2 in figure 5b, indicating that our desired polymer was made. However, the trace also showed a high molecular weight species. This could be due to some of the branching monomer being incorporated into the polymer with MA, creating branches off of those backbones. The more likely explanation though is that the chains are coupling to create larger polymers. However, once the branching monomer was incorporated into the backbone with IBVE, these issues were expected to decrease. Therefore, it was confirmed that MA branches can grow from the branching monomer randomly distributed throughout the backbone.

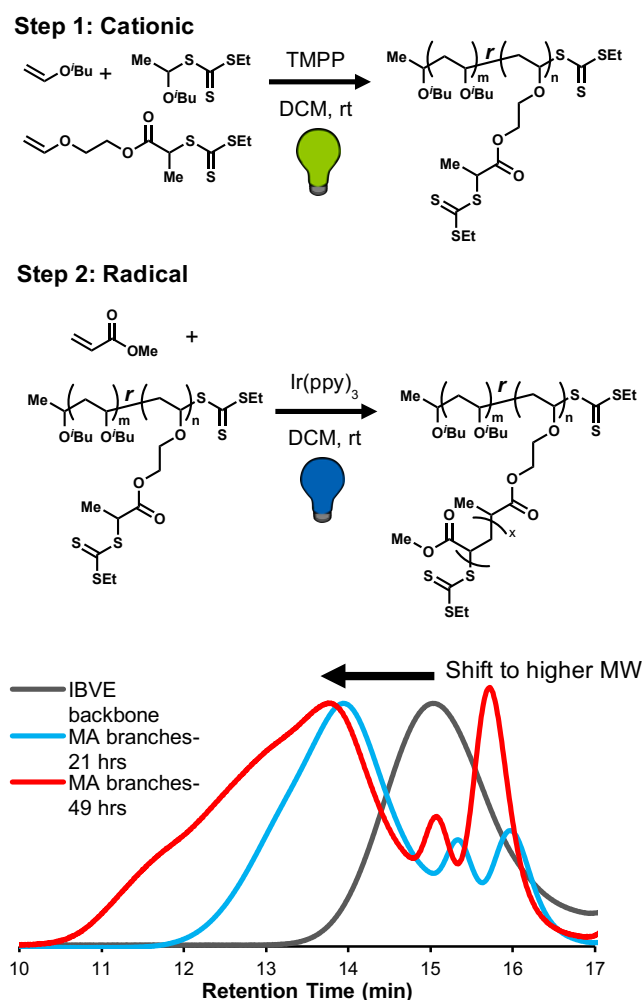


Figure 6. Stepwise polymerization of graft polymers. Step 1 is the cationic polymerization of IBVE and BM. Step 2 is the radical polymerization of MA.

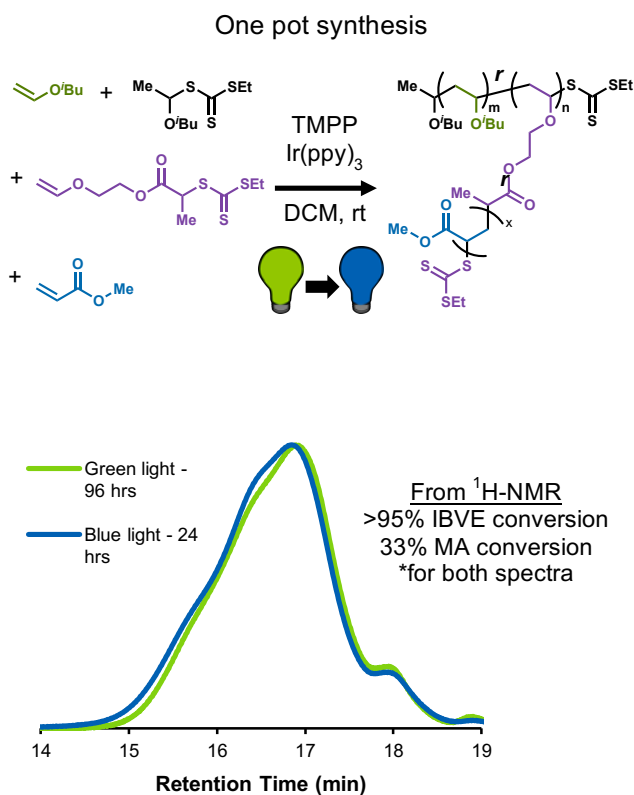


Figure 7. Attempt at the one pot synthesis of graft polymers. Under green LEDs, MA polymerized when it should not have since Ir(ppy)₃ does not absorb that wavelength. In addition, there is no change in the GPC trace after 24 hours under blue light.

The experiment shown in figure 6 tested the formation of graft polymers in a stepwise fashion. Similar to before, initiator, IBVE, BM, and TMPP were polymerized in DCM at room temperature under green light for 91 hours to obtain the backbone of the graft polymer. With good agreement between the experimental and theoretical molecular weights, MA and Ir(ppy)₃ stock solution were injected into the reaction vial to maintain an inert atmosphere. The vial was then placed under blue LEDs to initiate the radical polymerization of MA to form the branches of the graft polymer. After 21 hours, there was a clear shift in the GPC trace to higher molecular weights with 70% conversion of MA, most likely indicating that graft polymers were forming. However, there were also low molecular weight peaks present in the spectra, which were most likely the result of excess branching monomer that was not fully polymerized into the backbone with IBVE, allowing it to initiate linear polymers of MA. By ¹H-NMR, MA reached full conversion after 49 hours. However, the desired peak in the GPC spectra broadens significantly, most likely due to coupling between the graft polymers. By stopping the polymerization of the branches earlier, there will still be the desired shift to higher molecular weights, while also maintaining a good dispersity. The lower molecular weight species present in the spectrum may be removed through methods such as precipitation to obtain the purified graft polymers.

With these results, the polymerizations were attempted in one pot (Figure 7). After 96 hours under green LEDs, the IBVE and BM had gone to full conversion. In addition to this, 33% conversion of MA was seen. This undesired polymerization should not have occurred as Ir(ppy)₃ does not absorb green light, so it cannot initiate polymerize. Therefore, the conversion of MA could be a result of auto-polymerization from insufficient cooling of the vial under the heat produced from the green LEDs. Despite these inconsistencies, the vial was placed under blue LEDs to initiate radical polymerization of MA from the branching monomers. However, after 24 hours, there was no change in the conversions determined by ¹H-NMR, and the GPC trace was essentially identical to the polymerization prior to irradiation with blue LEDs, demonstrating that no additional polymerization occurred under blue light. This could potentially be due to air leaking into the vial or be a result of Ir(ppy)₃ photo-bleaching after being exposed to green light for too long, preventing catalysis and polymerization of MA.

Conclusion While further optimization is needed on the one pot system, the preliminary results show promise for the development of a one pot system to form graft polymers through the interconversion of cationic and radical polymerizations using visible light. Other potential options include utilizing a branching monomer functionalized with an initiator for a different type of light-mediated controlled radical polymerization. By doing this, many of the issues with coupling and unwanted initiation of homopolymer from excess branching monomer in solution may be eliminated.

Acknowledgments Thank you to the entire Fors group, especially Dr. Brett Fors and Veronika Kottisch for providing priceless mentorship and support. Thank you to the CCMR REU program funded by NSF for allowing me the opportunity to participate in their summer program.

Funding Research reported here was supported by the National Institute of General Medical Sciences of the National Institutes of Health under Award Number T34GM113848.

References

1. Matyjaszewski, K. Graft Copolymers. <http://www.cmu.edu/maty/materials/Properties-of-well-defined-graft-copolymers%20%20.html> (accessed Aug 7, 2017).
2. <https://omnexus.specialchem.com/selection-guide/high-impact-polystyrene/copy-of-applications> (accessed Aug 7, 2017).
3. Bhattacharya, A. Radiation and industrial polymers. *Prog. Polym. Sci.* **2000**, *25*, 371 – 401.
4. Bhattacharya, A.; Misra, B. N. Grafting: a versatile means to modify polymers: Techniques, factors and applications. *Prog. Polym. Sci.* **2004**, *29*, 767 – 814.
5. Muramatsu, N.; Yoshida, Y.; Kondo, T. Possible Application of Polyamine Graft Copolymer to Target Drug Delivery. *Chem. Pharm. Bull.* **1990**, *38*, 3175 – 3176.

6. Pakula, T.; Zhang, Y.; Matyjaszewski, K.; Lee, H.-I.; Boerner, H.; Qin, S.; Berry, G. C. Molecular brushes as super-soft elastomers. *Polymer* **2006**, *47*, 7198–7206.
 7. Daniel, W. F. M.; Burdyńska, J.; Vatankhah-Varnoosfaderani, M.; Matyjaszewski, K.; Paturej, J.; Rubinstein, M.; Dobrynin, A. V.; Sheiko, S. S. Solvent-free, supersoft and superelastic bottlebrush melts and networks. *Nat. Mater.* **2015**, *15*, 183–9.
 8. Feng, C.; Li, Y.; Yang, D.; Hu, J.; Zhang, X.; Huang, X. Well-defined graft copolymers: from controlled synthesis to multipurpose applications. *Chem. Soc. Rev.* **2011**, *40*, 1282–1295.
 9. Kottisch, V.; Michaudel, Q.; Fors, B. P. Photocontrolled Interconversion of Cationic and Radical Polymerizations. *J. Am. Soc. Chem.* **2017**, *ASAP*.
-

Non-enzymatic Glycation Enhances Mechanical Properties of Collagen Bioinks for 3D Printing

Leigh Slyker¹, Nicole Diamantides², and Lawrence Bonassar²

¹The University at Buffalo (SUNY), Buffalo, NY, ²Cornell University, Ithaca, NY

Abstract

Collagen has been widely explored as a potential bioink for extrusion-based bioprinting. However, weak mechanical properties and low printability relative to other hydrogels restrict the potential of collagen in 3D bioprinting. This study investigated the effect of non-enzymatic glycation of concentrated collagen hydrogels with 125, 250, and 500 mM ribose on rheological properties and printability of the gel. Our results showed that addition of ribose increased initial and final rheological properties, while adversely affecting gelation kinetics. Overall, glycation had no significant effect on printability of the gel, as determined by dot footprint area.

Introduction

Collagen has potential as a bioink due to its natural cell binding sites, enzymatic degradability, and low immunogenicity [1]. However, collagen hydrogels exhibit weaker mechanical properties and slower gelation compared to other natural and synthetic hydrogels. Previous work from our group found that photo-crosslinking of collagen gels with riboflavin improved mechanical properties and printability. Yet, due to the photo-crosslinking process, cell viability and uniformity of crosslinking suffered [2]. Non-enzymatic glycation of 1.5 mg/mL collagen hydrogels using ribose likewise improved mechanical properties of the gel, while adversely affecting gelation kinetics, and with no effect on cell viability [3,4]. Given the potentially conflicting effects of gel mechanics and gelation kinetics on printability, this study aimed to investigate the effect of non-enzymatic glycation on printability and stiffness in concentrated collagen gels of 8 mg/mL and ribose concentrations up to 500 mM.

Materials and Methods

Collagen Gels

Rat tail tendon-derived type I collagen was solubilized in 0.1% acetic acid at a concentration of 150 mg/g of tendon for at least 48 hrs at 4°C. Solutions were then centrifuged at 9000 rpm for 90 minutes. The resulting supernatant was frozen, and lyophilized for 96 hours. Collagen stock was then prepared through reconstitution of the lyophilized collagen in 0.1% acetic acid at a concentration of 15 mg/mL collagen.

Hydrogels were prepared by neutralization using a solution of 1M NaOH and 1X phosphate buffered saline (PBS) and 10X PBS, as described previously [2]. Glycated collagen gels were prepared by mixing 1.5 M ribose in 0.1% acetic acid with 15 mg/mL collagen stock to final concentrations of 125, 250, and 500 mM ribose and 8 mg/mL collagen. Collagen-ribose solutions were left at 4°C for 5 days to ensure complete glycation and all solutions were kept on ice before mixing.

Rheological Characterization

Rheological measurements were performed on an Anton Paar MCR 501, as described previously, using a 25 mm parallel plate geometry. Glutaraldehyde treated glass coverslips were attached to each rheometer plate to prevent wall slip during testing. Each coverslip was treated with 1% polyethyleneimine (PEI, Sigma, St. Louis, MO) for 10 minutes, rinsed with deionized (DI) water, then treated with 0.1% glutaraldehyde (GA, Sigma, St. Louis, MO) for 30 minutes, before rinsing three times with DI water [4].

Rheological testing consisted of 5 minutes at 4°C followed by 30 minutes at 37°C, to induce gelation [4]. Storage (G') and loss (G'') moduli were recorded over the testing period. Gelation time was determined as the point at which storage modulus surpassed loss modulus.

Printability Assessment

Printability was assessed using a Fab@Home extrusion-based 3D printer from Seraph Robotics with a temperature-controlled print pad. Collagen solutions were loaded into a 10 mL syringe equipped with a 0.25 mm tapered nozzle (Nordson EFD, East Providence, RI). Dots of various volumes (0.01-0.1 mL) were then dispensed onto a glass plate held at 37°C. The footprint areas of printed dots were obtained using ImageJ and MATLAB, as described previously [4].

Statistical Analysis

One way ANOVA with post-hoc Tukey HSD was used to determine the effect of ribose

concentration on initial and final storage and loss moduli, as well as on dot footprint area. All graphical data is reported as mean \pm standard deviation.

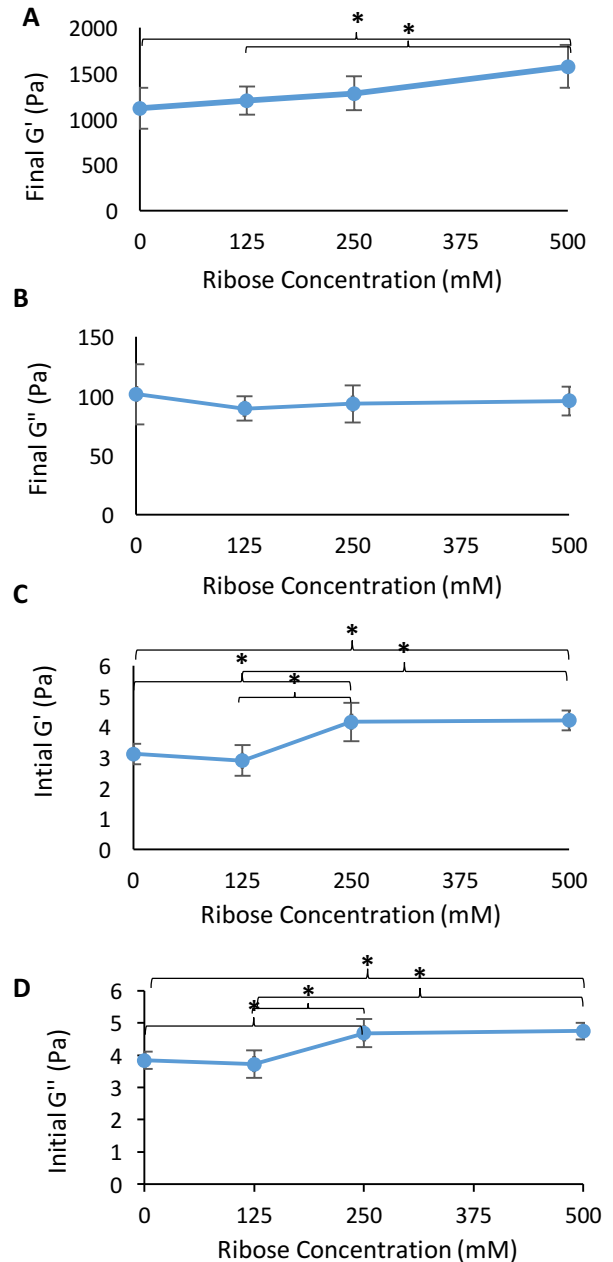


Figure 1. (A) Final storage modulus (G') for collagen gels with varying ribose concentration (mM). (B) Final loss modulus (G''). (C) Initial storage modulus (G'). (D) Initial loss modulus (G''). * indicates significant difference ($p < 0.05$).

Results

Collagen gels glycated with 125, 250, and 500 mM ribose showed increased storage and loss moduli in their un-gelled state, compared to collagen controls. Upon gelation, glycated collagen exhibited increased storage modulus with increasing ribose concentration (Figure 1A), while glycation had no significant effect on loss modulus in the gelled state (Figure 1B). Glycated collagen gels also underwent sol to gel transition later than collagen controls (Figure 2A). Observed dot footprint areas were consistently 10% lower for 500mM than in the control, however there was no statistically significant effect of ribose concentration on dot footprint area (Figure 2B). Thus, although the gelation took longer in glycated gels, printability did not suffer as a result.

Discussion

These results indicate that glycation increases the mechanical properties of the gel for collagen concentrations of 8 mg/mL. Similar trends were previously found in collagen concentrations of 1.5 mg/mL [2,3].

As initial printability is correlated with initial rheological properties [4], these results point to possible increases in printability with addition of ribose. Unfortunately, increases in gelation time negatively impacted printability with addition of ribose. As a result, there was no significant effect on printability.

Acknowledgements: This work was supported by the Cornell Center for Materials Research with funding from the Research Experience for Undergraduates program (DMR-1460428 and DMR-1120296). Additionally, this work made use of the Center for Nanomaterials Engineering & Technology shared research facilities at Cornell University.

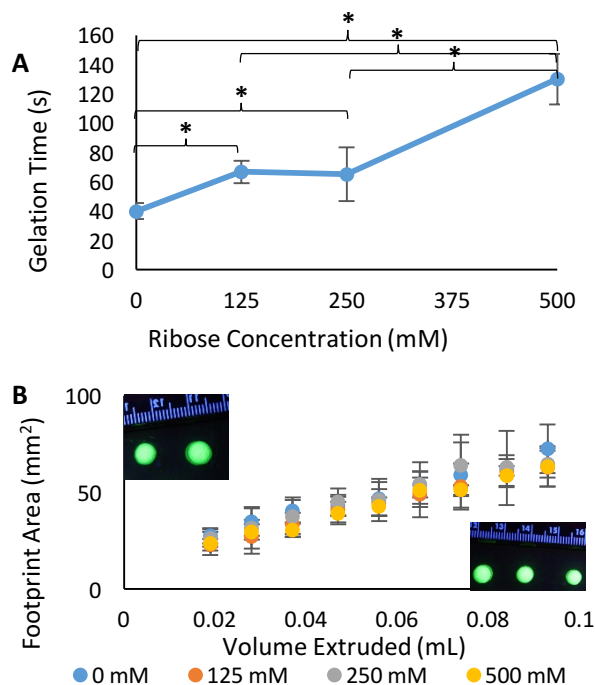


Figure 2. (A) Gelation time with varying ribose concentration (mM), calculated as time of crossover of loss modulus (G'') by storage modulus (G'). (B) Dot footprint area for varying volumes extruded, for varying ribose concentration.

Conclusions:

This study shows that glycation of collagen gels with ribose increases mechanical properties in both the sol and gel states. Although gelation time increased with addition of ribose, there was no significant increase in dot footprint area, and thus no decrease in printability of the gel. Future studies might aim to improve printability alongside mechanics through addition of higher ribose concentrations.

References:

1. Helary, C., *Biomaterials*, 2010, 31, 481-490;
2. Mason B.N., *Acta Biomater*, 2013, 9, 4635-4644;
3. Roy, R., *J. Orthop. Res.*, 2008, 26, 1434-1439;
4. Diamantides, N., *Biofabrication*, 2017, 9, 034102

Synthesis of Asymmetric Block Copolymers Containing Stable Radicals

Sarah Timmins¹, Alicia Cintora², Christopher Ober²

¹Department of Materials Science and Engineering, Clemson University, Clemson, SC 29631

²Department of Materials Science and Engineering, Cornell University, Ithaca, NY 14853

ABSTRACT

Block copolymers containing stable radical groups have emerged as promising materials for use in organic electronics because of their redox activity. Research into their use has been plagued by a number of issues that have been difficult to correct due to a lack of understanding of the charge transport mechanism within these polymers. This project examined the formation of microstructures within asymmetric poly(2,2,6,6-tetramethyl piperidinyloxy)-*b*-poly(2,2,2-trifluoroethyl methacrylate). The copolymers were synthesized using anionic polymerization and thin films were spun coated onto silicon wafers. The coated wafers were annealed thermally as well as by vapor anneal in a variety of solvents and micro-structure formation was analyzed using atomic force microscopy (AFM).

I. INTRODUCTION

As society becomes increasingly technologically driven, the need for better battery technology has become more important than ever. The market demands powerful, lightweight batteries with minimal recharging time. Extensive research has been conducted on the use of nitroxide-bearing block copolymers in energy storage devices, but these devices are not without issue. They suffer from a low number of cycles, degrading charge capacity, and a dependence on additives to achieve desirable properties.¹⁻³ Paramount to engineering better systems is understanding the relationship between orientation of the microstructures and conductivity.

A useful feature of block copolymers is their ability to self-assemble into ordered structures. This process, known as phase separation, is driven by the enthalpy of de-mixing for the blocks. The phase structure of the block copolymers is a function of only three variables: the volume fraction of the first component (f_A), the degree of polymerization (x), and the Flory-Huggins polymer-polymer interaction parameter χ . The transition to heterogeneous microphases is known as the order-disorder transition, and the mean-field approach can be used to evaluate the dependence of this transition on f_A and χ . From this information, the morphology diagram in Figure 1 can be constructed. Structures

formed in the BCC and HEX regions of Figure 1 result in spherical and cylindrical micro-structures, respectively.⁴

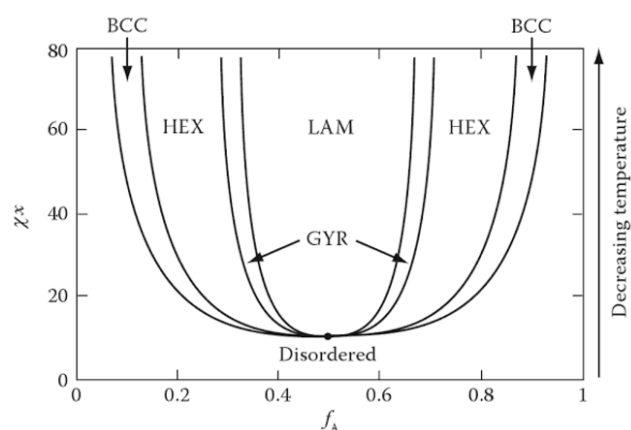


Figure 1. Block copolymer morphology diagram for a di-block copolymer.

Since 2002, there has been much work done on the use of block copolymers containing 2,2,6,6-tetramethyl piperidinyloxy (TEMPO) and their use in energy storage systems.⁵ More recent research suggests that introduction of a fluorinated group within the block copolymer increases the degree of phase separation compared to a similar polymer without the fluorinated block.⁶

II. EXPERIMENTAL

Purification of dibenzo-18-crown-6 (DB18C6)

Purification of DB18C6 was accomplished by recrystallization. First, 3 g of DB18C6 was weighed into a flat round bottom flask and suspended in 70-mL of acetonitrile. The mixture was stirred at 90°C for 1 h until fully dissolved. The solution was left to cool slowly to room temperature and then placed into the freezer for 24 h before being collected by filtration.

*General Synthesis of PTMA-*b*-PTFEMA*

To begin, 0.126 g of DB18C6 was weighed into a 250-mL Schlenk flask. A stir bar was added and the flask was allowed to pump into the glove box for 15 minutes. The stop cock was installed and opened only enough for a needle to be inserted. Using a syringe, 45-mL of distilled THF was added to the reaction flask. The unsealed neck was then sealed using septa and parafilm before the flask was removed from the glove box. The reaction flask was transferred to a stir plate. The neck and the entire flask were purged using Argon gas. The mixture was allowed to stir until the DB18C6 was fully dissolved. With the stop cock closed, the flask was transferred to a dewar containing acetone, to which dry ice was added until the mixture reached equilibrium at -78°C. Meanwhile, *sec*-BuLi was pumped into the glove box for 15 min. Using a 1-mL syringe, 0.5-mL of *sec*-BuLi was measured out and the needle was purged in THF. A long needle was attached and plugged with a piece of septa, while the joint was sealed with parafilm. The syringe was removed from the glovebox and the *sec*-BuLi was added to the reaction mixture dropwise. The needle was purged with THF. The reaction flask was removed from the bath and allowed to warm to room temperature while the bath was covered with aluminum foil. Once at room temperature, the flask was placed back into the bath and allowed to cool for 15 min. In the glove box, a syringe containing 0.1-mL of DPE was prepared and removed. Once cooled, the correct amounts of DPE and then *sec*-BuLi were added to the reaction flask. The dewar was covered with aluminum foil and left to sit for 30 min. The correct amount of *tert*-BuONa was measured out and added at the end of 30 min. The Schlenk flask containing the monomer should be wiped using acetone and pumped into the glove box for 30 minutes. Inside the glove box the correct amount of TEMPO-methacrylate was

measured out, removed, and then added to the reaction flask. The monomer was left to react for 15 hours. A 20-mL vial was charged with methanol, connected to argon gas and allowed to bubble. A needle and syringe were purged with argon gas while the TFEMA pumped into the glove box for 15 minutes. The appropriate amount of TFEMA was measured out. Using the purged needle, 5-mL of the reaction mixture was removed and added to the bubbling methanol. The TFEMA was added to the reaction mixture and left to react for 15 min. Meanwhile, a needle and syringe was purged and another flask of methanol was bubbled. When the reaction was finished, it was quenched by adding 1-mL of methanol to the reaction flask using the purged needle and syringe.

Washing of the Collected Polymer

The 20-mL vial containing the homopolymer collected before addition of the second monomer was prepared for collection by sealing with an upside-down septa and tape. The small bump trap was installed on the rotovap; a needle was inserted through the septa and the vial was affixed to the bump trap. The column on the rotovap was filled with liquid nitrogen and the temperature of the water bath was set to 30°C. After rotovapping, the resultant solid was suspended in 5-mL of DI water and 5-mL of chloroform and allowed to separate. The polymer was washed twice with DI water. After the final wash, the solution was suspended in a 20-fold amount of hexanes, covered with aluminum foil, and left to stir for 30 minutes. After 30 min, the solution was cooled in a dewar containing liquid nitrogen and filtered using a vacuum filtration. The polymer was then dried overnight in a vacuum oven at 45°C.

Washing of Block Copolymer

After quenching, the reaction mixture was rotovapped to remove any solvent. The resultant solid was suspended in chloroform and washed with water 3 times in a separatory funnel. The washed solution was suspended in 20-fold of hexanes and stirred for 30 minutes. The solution was then cooled in a liquid nitrogen bath and collected via vacuum filtration.

Spin Coating of Polymer Samples

Spin coating was performed using a 2 wt% solution of polymer in α - α - α trifluorotoluene, prepared from 125 mg of polymer in 5-mL (5.95 g) of α - α - α trifluorotoluene. The silicon wafer was first coated in quarters; a quarter wafer was placed on the coater and sealed by vacuum. The wafer was cleaned by spinning at 1000 RPM for 30 s at 400 RPM/s with α - α - α trifluorotoluene. After applying the 2 wt% solution, the wafer was spun again for 30 s at 1000 RPM and 400 RPM/s. The coated wafer was prepared cut into smaller pieces.

Annealing of Spin Coated Samples

The spin coated samples were annealed at 100°C for 1 h, 3 h, and 24 h as well as at 150°C for 1 h and 3 h. Vapor anneals were done for 24 h in acetone, chloroform, toluene, dichloromethane, 1,2-dichloroethane, 1,1,2,2-tetrachloroethane, 1,1,1-trichloroethane, and α - α - α trifluorotoluene. Additional vapor anneals were performed in chloroform for 30 min, 1 h and 3 h. The use of solvent mixtures for vapor anneals was also explored using 1:1 mixtures of toluene and dichloromethane, toluene and α - α - α trifluorotoluene, and toluene and chloroform. All anneals were performed in glass petri dishes, and vapor anneals were done using 10-mL of solvent.

III. RESULTS

Each of the block copolymers and homopolymers were analyzed using GPC to determine molecular weights. A graph of the GPC data for the block copolymers is given in Figure S1. From this information, the amount of each block was calculated. This data is presented in table 1.

Table 1. Polymer Molecular Weight Data

	PTMA	PTFEMA	M_n [g/mol]	\bar{D}	Fluorine content
1	6,600	29,000	35,600	1.19	81%
2	7,700	22,400	30,100	1.18	74%
3	33,300	7,300	40,600	1.18	18%
4	33,900	3,300	37,200	1.18	9%

Once the polymers had been spin coated onto wafers, they were annealed as described and characterized through AFM. Some images displaying the transition from order to disorder are shown in Figure 2.

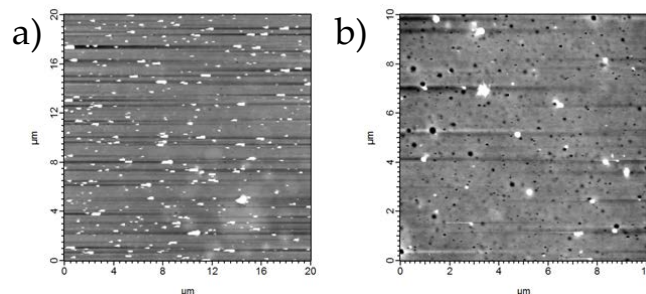


Figure 2. AFM images describing the transition from order to disorder in a PTMA-*b*-PTFEMA copolymer that is 9% PTFEMA. a) an unannealed wafer, and b) a wafer after annealing for 24h at 100°C.

A catalog of images showing the formation of structures in all of the produced polymers are provided in the supplemental information as figure S2.

IV. DISCUSSION

The results of the AFM characterization show the formation of cylinders in all of the prepared thin films. However, the cylinders lacked uniformity in size and long range order. Moving forward there are multiple possible routes worth investigating in order to produce more uniform structures. One possibility is that the prepared films were too thick, causing the low surface energy fluorinated block to phase separate onto the surface. The use of solvent mixtures was investigated towards the end of the summer with some interesting results. Further exploration using a larger array of solvent combinations could yield better structure formation. Another possible improvement would be sealing the glass petri dishes using a grease seal in order to prevent the solvent from evaporating. Additionally, a method known as guided self-assembly, in which the surface energies of the silicon wafer are altered to cause the formation of specific microstructures.

V. CONCLUSION

Nitroxide-bearing block copolymers have been extensively studied for their use in energy storage devices. Block copolymers like the ones synthesized

for this project can undergo phase separation during annealing if the chains have sufficient mobility. The synthesis of asymmetric PTMA-*b*-PTFEMA yielded polymers that formed cylindrical structures upon vapor annealing. However, these structures lacked uniformity and order and thus further attempts will be required to achieve the quality structures needed for electrical characterization of PTMA-*b*-PTFEMA.

VI. ACKNOWLEDGEMENTS

I would like to thank Dr. Christopher Ober and Alicia Cintora, as well as the entire Ober Research Group for their support on this project. I would also like to thank the NSF REU Program (DMR-1460428 and DMR-1120296) and the Cornell Center for Materials Research.

VII. REFERENCES

1. Nakahara, K.; Iwasa, S.; Satoh, M.; Iriyama, J.; Suguro, M.; Hasegawa, E. *Chem. Phys. Lett.* **2002**, *359* (5), 351–354.
2. Nakahara, K.; Iriyama, J.; Iwasa, S.; Suguro, M.; Satoh, M.; Cairns, E. J. *Journal of Power Sources* **2007**, *163*(2), 1110–1113.
3. Nishide, H.; Iwasa, S.; Pu, Y.-J.; Suga, T.; Nakahara, K.; Satoh, M. *Electrochimica Acta* **2004**, *50*(2–3), 827–831.
4. Young, R. J.; Lovell, P. A. *Introduction to Polymers*, 3rd ed.; CRC Press: Boca Raton, 2011.
5. Janoschka, T.; Hager, M. D.; Schubert, U. S. *Advanced Materials* **2012**, *24* (48), 6397–6409.
6. Liedel, C.; Moehle, A.; Fuchs, G. D.; Ober, C. K. *MRS Communications* **2015**, *5* (03), 441–446.

SUPPLEMENTAL INFORMATION

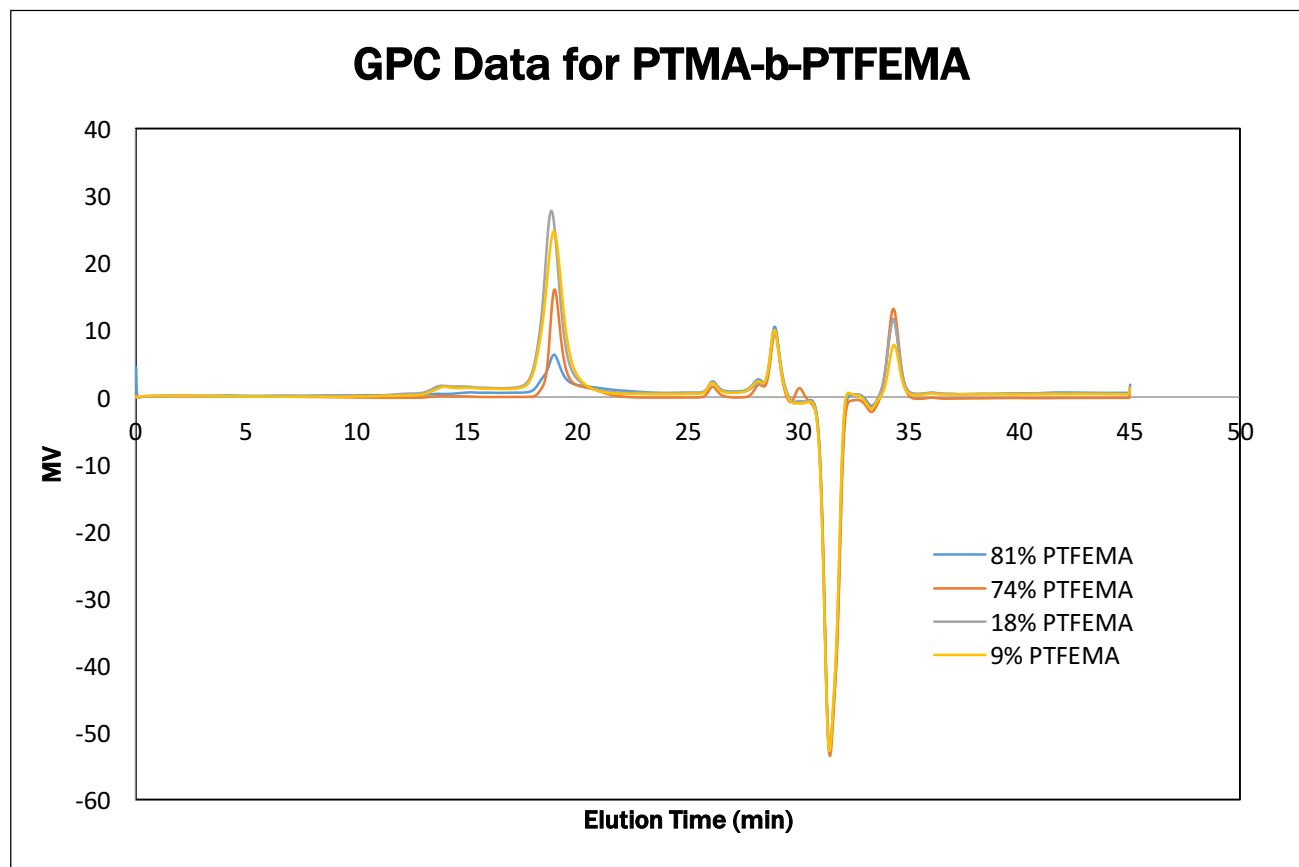
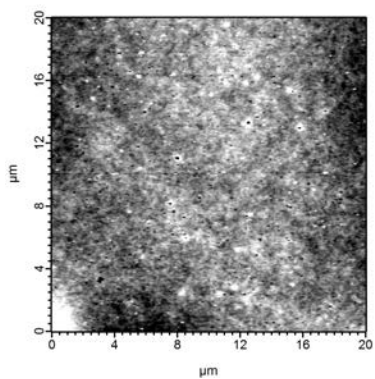
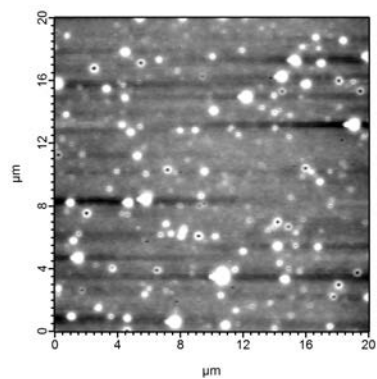


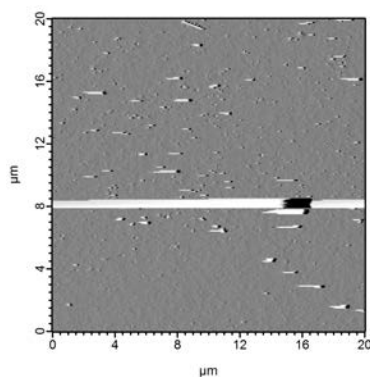
Figure S1. GPC curves for PTMA-*b*-PTFEMA copolymers synthesized at 81%, 74%, 18%, and 9% PTFEMA.



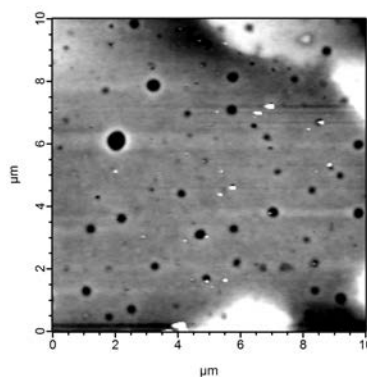
a) 81% PTFEMA, unannealed



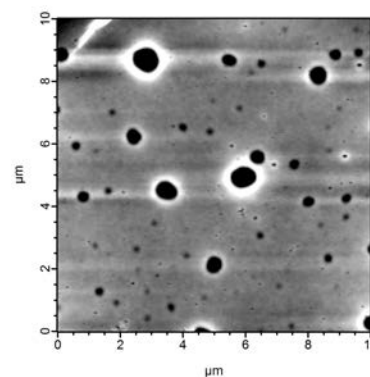
b) 81% PTFEMA, 100°C 24 h



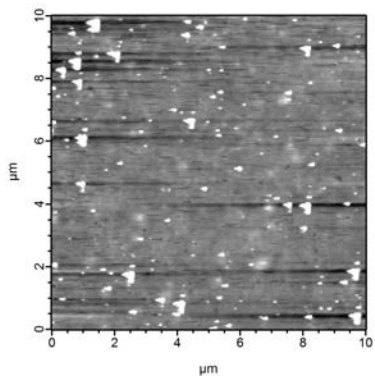
c) 74% PTFEMA, unannealed



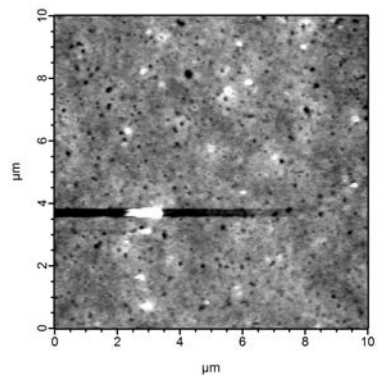
d) 74% PTFEMA, 1,1,2,2-tetrachloroethane



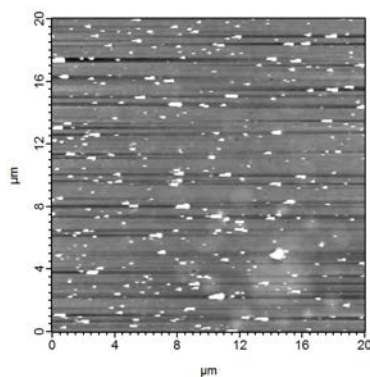
e) 74% PTFEMA, acetone 24 h



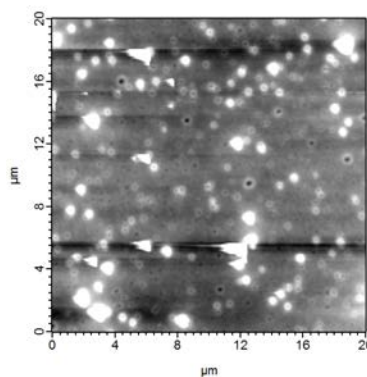
f) 18% PTFEMA, unannealed



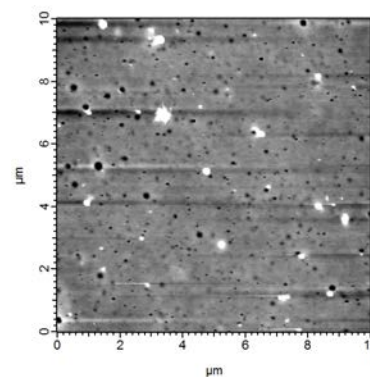
g) 18% PTFEMA, acetone 24 h



h) 9% PTFEMA, unannealed



i) 9% PTFEMA, CHCl₃ for 24 h



j) 9% PTFEMA, 100°C 24 h

Figure S2. AFM images of annealed and unannealed polymer films.

Statistical Prediction of Polymer Properties Based on Molecular Weight Distribution

Erika S Tirado, Junteng Jia, and Robert A Distasio Jr

Department of Chemistry and Chemical Biology, Cornell University, Ithaca, NY 14853, USA

Abstract: It has been hypothesized and observed that varying molecular weight distributions (MWDs) affects polymer properties^{1,2}, but this relationship remains relatively difficult to identify for different polymers and different properties. There have been recent studies developing methods that yield unprecedented control over the shape of a polymer's MWD. Having such control over the MWDs, we would like to now develop an accurate and reliable theoretical approach for predicting their properties. In this work, we directly address this challenge by utilizing tools from population statistics, least squares analysis, and machine learning to develop a predictive model for a series of different physical properties of interest based on the central moments of polymer MWDs. Our approach shows high fidelity to the available experimental data and represents an unexplored avenue toward the synthesis of polymers with targeted properties and functionalities.

Background and Model: Two of the most common ways of characterizing polymers and identifying the effect of their MWD on their properties are the number average molecular weight (M_n) and the weight average molecular weight (M_w)⁴. When looking at raw Chromatography data one can obtain the number average molecular weight (M_n) of a given distribution μ by simply looking at the first statistical moment of the molecular weight distribution, which is defined in Equation 1 below.

$$M_n^{(\mu)} = M_1^{(\mu)} = \int \rho(t; \mu) t dt \quad (1)$$

in which $\rho(t; \mu)$ stands for the probability density of finding a specific polymer length at a given time t . We obtain the probability density at a given retention time as described by Eq. 2,

$$\rho(t) = \frac{\Delta n(t)}{\int \Delta n(t) dt} \quad (2)$$

in which $\Delta n(t)$ describes the baseline-corrected refractive index information at a given time t . We can do this because it is a known fact that the refractive index is proportional to concentration.

Since intuition and experience tells us that it is possible to characterize polymer properties based on M_n , which can be described using the first statistical moment of a polymer MWD, we decided to look at the following quantities based on the second and third central moments of these MWDs which we define as follows:

$$M_2^{(\mu)} = \sqrt{\int \rho(t; \mu) (t - M_1^{(\mu)})^2 dt} \quad (3)$$

and,

$$M_3^{(\mu)} = \int \frac{\rho(t; \mu) (t - M_1^{(\mu)})^3 dt}{M_2^{3(\mu)}} \quad (4)$$

Equation 3 describes the square root of the second central moment of a distribution, which describes the standard deviation with respect to the the mean of a specific distribution. In other words, the spread of the distribution describes how narrow or wide it is. When the spread goes down the distribution is narrower, when the spread goes up the distribution is wider.

Equation 4 utilizes the third centralized moment of a distribution divided by $M_2^{3(\mu)}$ which describes the skewness of given distribution μ . The skewness of a distribution describes the behavior of the distribution's tail. If the tail of a distribution extends left (right) then the skewness is negative (positive).

Once a method to describe the shape of a MWD curve has been defined with the statistical moments, we can use least square analysis to understand the relationship between the MWD of a polymer and its properties and subsequently predict polymer properties by using their MWDs. To do so we must compare multiple molecular weight distributions from the same polymer to each other to understand exactly how they differ from one another and the ways in which their differences affect their properties. To do this we define a population mean for every observable feature as follows:

$$\overline{M}_q = \frac{1}{T} \sum_{\mu=1}^T M_q^{(\mu)} \quad (5)$$

in which \overline{M}_q is the population mean of the q^{th} moment with respect to all T training samples. Using this we can define how individual MWD moments deviate from the population mean as follows:

$$\Delta M_q^{(\mu)} = \frac{M_q^{(\mu)} - \overline{M}_q}{\overline{M}_q} \quad (6)$$

Once we have each moment's deviation the population mean we can put that information into our linear squares analysis model.

Least squares analysis works with the assumption that there is a linear relationship between our observable features and the properties we want to predict as follows:

$$Ax = b \quad (7)$$

where A is a matrix with the observable features in the rows, and each column holds the observables for each set of data we're looking at. In this case the observables are the moments of our distributions and the sets of data are the distribution curves themselves. x is a coefficient vector that describes the relationship between A and b, and b is the given property we are trying to predict.

To train our prediction model and understand the relationship between our moments and our properties we solve Eq. 7 for a coefficient vector x so that the square of the 2-norm of the error is minimized.

$$x = \arg \min_x \|Ax - b\|_2^2 \quad (8)$$

The 2-norm squared term of equation 8 can be written as,

$$\|Ax - b\|_2^2 = (Ax - b)^T (Ax - b) = x^T A^T A x - 2x^T A^T b + b^T b \quad (9)$$

To minimize the above term, we take the variational derivative with respect to x of the equation and set it to zero as such:

$$2\delta x^T A^T A x - 2\delta x^T A^T b = 0 \quad (10)$$

Which leads us to the solution of the least square fit.

$$x = (A^T A)^{-1} A^T b \quad (11)$$

Equation 11 can be translated in the terms of our prediction model as fitting a polymer's desired property to a power series expansion formula such as

$$\eta^{pred,\mu} = \sum_{i+j+k=0}^p \phi_{ijk} [\Delta M_1^{(\mu)}]^i [\Delta M_2^{(\mu)}]^j [\Delta M_3^{(\mu)}]^k = \sum_{i+j+k=0}^p \phi_{ijk} f_{ijk}^{(\mu)} \quad (12)$$

To be able to physically interpret our training coefficients, we will normalize $\{f_{ijk}^{(\mu)}\}$ as follows:

$$\overline{f_{ijk}^{(\mu)}} = \frac{f_{ijk}^{(\mu)}}{\max(\{f_{ijk}^{(\mu)}\})} \quad (13)$$

Using this normalized information, we can rewrite our prediction model as

$$\eta^{pred,\mu} = \sum_{i+j+k=0}^p \phi_{ijk} f_{ijk}^{(\mu)} = \sum_{i+j+k=0}^p \bar{\phi}_{ijk} \overline{f_{ijk}^{(\mu)}} \quad (14)$$

We can understand this prediction model based on the principal definition of a linear relationship in equation 7, in this case A is $\overline{f_{ijk}^{(\mu)}}$, x is $\bar{\phi}_{ijk}$, and b is $\eta^{pred,\mu}$.

In case the least square analysis method seems to suggest a strong relationship between observables and the predicted properties, but exhibits signs of overfitting, we may want to regularize our results using a ridge regression, which expands upon the least squares fitting method by adding a constraint on the fitting coefficient. When adding a constraint to equation 8 it looks like this:

$$x = \arg \min_x (\|Ax - b\|_2^2 + \lambda \|x\|_2^2) \quad (15)$$

where λ , is our constraint factor. Solving this the same way we did above from equation 8 to 11 we get the resulting definition for our prediction coefficients:

$$x = (A^T A + \lambda I)^{-1} A^T b \quad (16)$$

Training and Testing Method: Given the refractive index from the chromatograms of N polymers along with their corresponding physical properties, we separate them into two groups, a training set, and a testing set. N-1 samples are assigned to the training set and the Nth remaining sample is assigned to the testing set. The model is fed the training data with both the polymer's MWD's moments and the physical property we are interested in, while for the testing set the model receives only the MWD's moments and it must use the information from the training data to calculate an appropriate fitting coefficient that will result in the prediction with the least square error while still satisfying the ridge regression constraint as seen below:

$$\{\phi_{ijk}\} = \arg \min_{\{\phi_{ijk}\}} \left[\sum_{\mu=1}^{N-1} (\eta^{pred,\mu} - \eta^{true,\mu})^2 + \sum_{i+j+k=0}^p \lambda \bar{\phi}_{ijk}^2 \right] \quad (17)$$

Equation 17 is the translation of equation 16 into the physical terms of the polymers we are working with. Where $\eta^{pred,\mu}$ is our predicted physical property from equation 14, and $\eta^{true,\mu}$ is our actual measured polymer property. By setting $p=2$, we include all the linear, coupling interaction, and quadratic terms, along with a constant term in the power expansion.

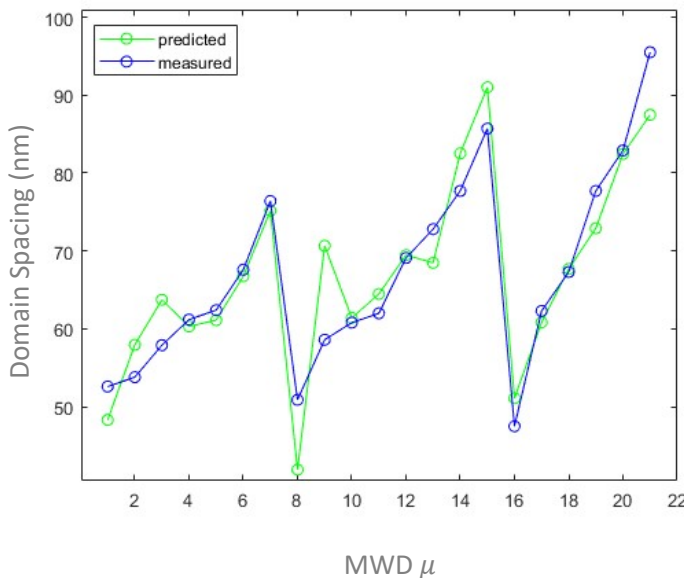


Fig. 1 Least square analysis model results.

Data Set 1: We were give two sets of molecular weight distributions of polymers along with their properties. The first set we looked at was a set of 21 molecular weight distributions of block copolymers and their domain spacing information.

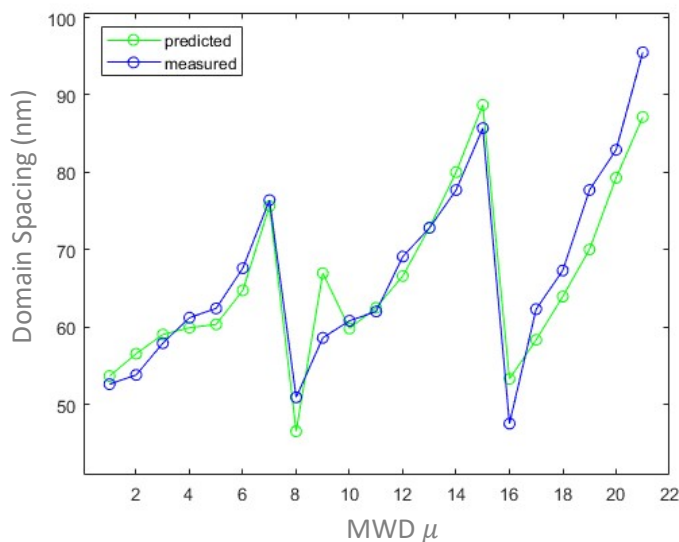
First, we tested our least square analysis on this data and out results are shown in Fig. 1 with the coefficient run-down on Table 1 and error analysis found in Table 2.

When examining all the fitting coefficients for all the training-testing data combinations we noticed that the y varied too much from one training set to another, suggesting that the least square analysis was overfitting the data, resulting in fitting coefficients that did not translate into a physical, rational relationship between the polymers MWD and its physical properties. When adding a ridge regression constraint, we obtained the results seen in Fig. 2 with the coefficient run-down on Table 3 and error analysis found in Table 4.

ijk	ϕ_{ijk}^{RG}
0 0 0	62.1329
1 0 0	-20.7795
2 0 0	2.6127
0 1 0	7.4069
1 1 0	-9.0489
0 2 0	7.1492
0 0 1	-1.816
1 0 1	-1.2719
0 1 1	1.3203
0 0 2	1.8799

error	nm
MSE	0.1421
MAE	3.6280
RMSE	4.8949
MAXE	12.0581

Left: Table 1, coefficient values for prediction of domain spacing LS. **Above:** Table 2, corresponding error.



ijk	ϕ_{ijk}^{RG}
0 0 0	62.1329
1 0 0	-20.7795
2 0 0	2.6127
0 1 0	7.4069
1 1 0	-9.0489
0 2 0	7.1492
0 0 1	-1.816
1 0 1	-1.2719
0 1 1	1.3203
0 0 2	1.8799

error	nm
MSE	-0.8089
MAE	3.1824
RMSE	4.0277
MAXE	8.3552

Above Left: Fig 3, ridge regression analysis model results.

Above Right: Table 3, coefficient values for prediction of domain spacing RR.

Left: Table 4, corresponding error.

Analysis of Results: We used the ridge regression method not only as a prediction tool but as a cross-validation tool to make sure we had chosen good observable features to describe the relationship of the MWD to the polymer's physical properties.

Looking at the fitting coefficients for the ridge regression model on table 3 we can look at specifically the first, second, fourth, and seventh rows to get a better understanding of the relationship between the MWD of a polymer and its physical properties as described by this model. The first row stands for the average mean domain spacing, it is the domain spacing the model would have guessed had it not had any information other than a constant. The second row stands for the relationship between the mean of the distribution and the domain spacing, a large negative number describes a strong inverse relationship, as the MWD average goes to a higher retention time, then molecular weight goes down and domain spacing goes down, as we expect from intuition. The fourth row describes that as the spread of the MWD goes up then so does domain spacing, which also makes sense per intuition. Lastly the 7th row suggests that as the tail extends left and we have a denser distribution at higher molecular weights our domain spacing goes up, as it has been suggested by a couple of studies.

Conclusion: Using least squares analysis and ridge regression we have modeled a way to predict polymer properties based on the MWDs. Our findings confirm widespread intuition about the effect of MWDs of polymers on their properties and it does so in a relatively easy to interpret way. This model used has shown an accuracy of up to 14% maximum error and may be used to look at different properties of polymers. In fact, this same model was tested with 22 different curves for a different polymer, this time testing the complex viscosity and the angular frequency at which storage and loss moduli equal each other with similar results.

Future work: This model can potentially be used to design MWDs of polymers that result in specific desired physical properties, which would make the production of desirable polymers easier. There is also the possibility of considering other ways to describe the shape of a MWD and map its relationship to physical properties of its polymers.

Acknowledgements: The study was supported by the Cornell Center for Materials Research and the National Science Foundation. Thanks to the Distasio Group for welcoming me into their space and their conversation and for preparing this project for me to work on. Thanks to the Fors group for meeting with us so often and so willingly answering our questions. Thanks specifically to Robert A. Distasio Jr. and Junteng Jia for their guidance and support.

References:

- (1) Gentekos, D.T.; Barteau K.P.; Fors, B.P. *In preparation*.
- (2) Kottisch, V.; Gentekos, D.P.; Fors, B.P. *ACS Macro Lett.* **2016**, 5, 796.
- (3) Gentekos, D.T.; Dupuis, L.; Fors, B.P. *J. Am. Chem. Soc.* **2016**, 138, 1848.
- (4) Rudin, A.; *J. Chem. Educ.* **1969**, 46, 595.

Flavin Catalysis

Celeste Tobar

Mount St. Mary's University, Los Angeles

CCMR REU

Summer 2017

August 09, 2017

Exploring Flavin Catalysis

Tobar, Celeste

Abstract:

Exploring the capabilities of flavin-catalyzed reactions, riboflavin tetraacetate was utilized as a catalyst that can facilitate hydrodebromination reactions by either reaction with BNAH or photoexcitation with blue LED light in the presence of formic acid and triethyl amine.

Introduction:

Flavins contain many properties: they are photoreceptors allowing them to absorb light and access their excited state and are capable of undergoing oxidation-reduction reactions. This quality is important because they can be used in reactions in small quantities and reused within the reaction. For this research, riboflavin tetraacetate ($\text{RF}(\text{OAc})_4$) was excited by shining a blue LED light (450nm) onto it. Although, when using 1-benzyl-1,4-dihydronicotinamide (BNAH) there is no need for photoexcitation since BNAH is a strong enough reducing agent. If a weaker reducing agent like formic acid (HCOOH) with triethylamine (Et_3N) is used, then there would be a need for blue LED light to be introduced since alone they will not be able to reduce $\text{RF}(\text{OAc})_4$. A photocatalytic cycle for the aerobic oxidation of various organic substrates with $\text{RF}(\text{OAc})_4$ was proposed by Bern Mühldorf¹ and Robert Wolf¹, in 2015 (figure 1).

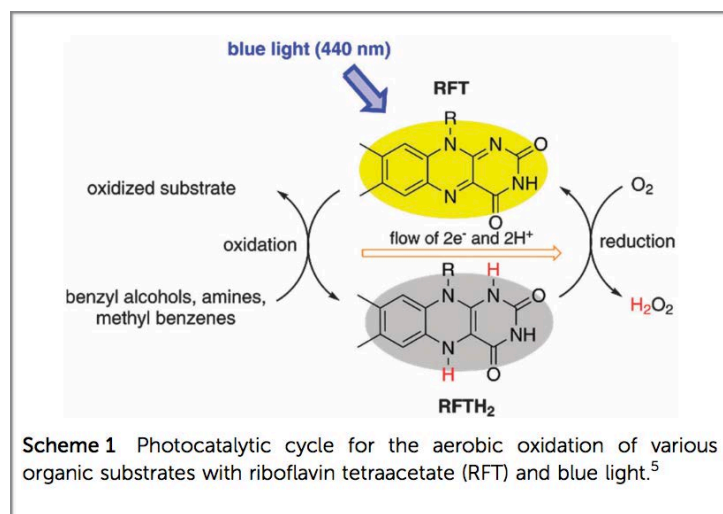
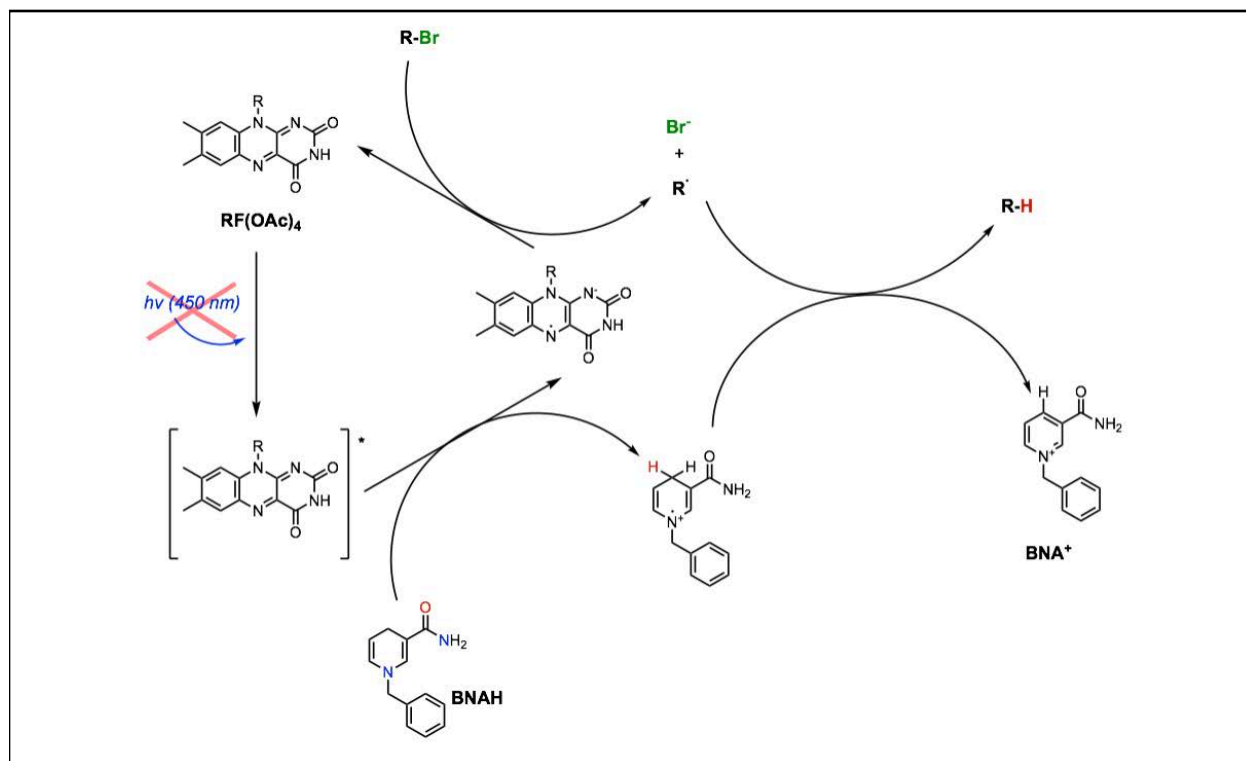


Figure 1. Photocatalytic cycle proposed by Bern Mühldorf and Robert Wolf

The proposed cycle involves an electron transfer followed by a proton transfer. For this research we will be exploring $\text{RF}(\text{OAc})_4$ -catalyzed reactions and the mechanism by which it operates.

Figure 2. Proposed mechanism



Alongside this, a detailed substrate scope will be carried out to investigate the reactions functional group tolerance.

Experimental:

Experimental set up when using BNAH as oxidizing agent

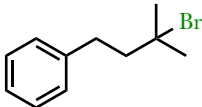
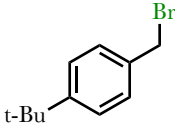
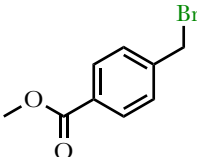
To a small vial was added brominated reagent (0.25 mmol), BNAH (65.2 mg, 0.3 mmol, 1.2 eq), RF(OAc)₄ (6.8 mg, 0.0125 mmol, 5 mol%), and a stir bar. The vial was then evacuated and backfilled with N₂ (3x). To this mixture was MeCN(0.25M, 1mL) and the resultant solution stirred at room temperature until completion (as judged by TLC analysis). The reaction was passed through a silica plug, dried with Na₂SO₄, filtered, and concentrated *in vacuo*.

Experimental set up when using HCOOH/Et₃N

To a small vial equipped with magnetic stir bar was added brominated reagent (0.25 mmol), HCOOH (20 μ L, 0.3 mmol, 1.2 eq), Et₃N (42 μ L, 0.3 mmol, 1.2 eq), RF(OAc)₄ (6.8 mg, 0.0125 mmol, 5 mol%), and a stir bar. The resulting solution was degassed *via* freeze-pump-thaw (3x). The solution was illuminated using blue LED light (450 nm) and allowed to store at room temperature until completion (as judged by TLC and analysis). To the solution was added H₂O (5 mL) and the organic layer was extracted with dichloromethane (3 x 15 mL). The organic layers were combined and washed with brine (5 mL), dried over Na₂SO₄, filtered, and concentrated *in vacuo*. The resulting crude products was purified *via* column chromatography.

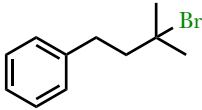
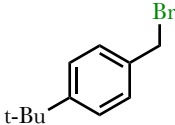
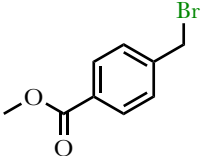
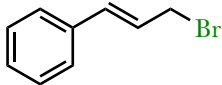
Results and Calculations:

Table 1: Results of reactions using BNAH

Bromide Substrate	Yield
	Product not isolated from substrates
	Product not isolated from substrates
	Trace Reactivity
	No Reaction
	No Reaction
	25% NMR Yield

* All reactions carried out on a 0.25 mmol scale of bromide substrate at 0.25M concentration.

Table 2: Results of reactions using HCOOH/Et₃N

Bromide Substrate	Yield
	Product not isolated from substrates
	Trace Reactivity
	No Reaction
	No hydride transfer product observed

* All reactions carried out on a 0.25 mmol scale of bromide substrate at 0.25M concentration.

Discussion:

The reactions carried out with BNAH and no blue led showed little to no conversion to the desired product, as seen in table 1. For those reactions that did show conversion isolation of the desired product proved troublesome due to similar R_f's between both starting materials and by products. It was confirmed *via* NMR analysis that various unidentifiable byproducts were formed during the course of the reaction, further inhibiting an accurate elucidation of the products structure. In future when performing these reactions we will test out other solvents and determine if they play a role in the overall reaction. As well as instead of just evacuating and backfilling the vial, freeze-pump-thaw could be utilized to ensure that there is no air within the vial. What was partially confirm by these reactions was that there was an electron and proton transfer as stated by the proposed photocatalytic cycle (see figure 2).

In the second set of reactions using HCOOH/Et₃N (shown on table 2) a similar trend in poor reactivity was observed as determined by both NMR and TLC analysis. Encouragingly through, product formation was observed *via* TLC visualization with UV and anisaldehyde. For one substrate, the debromination product could not be isolated from unwanted byproducts, because the starting material and the desired product are similar in polarity, meaning that their separation *via* column chromatography was difficult. Something to try in future reactions is simple distillation, although the scale in which these reactions were done on was a bit small for distillation, it could be accommodated on a larger scale.

Overall, the results were not that of what was expected but they did give an insight into the proposed mechanism, because there is some conversion of starting material. Both reactions still show promise in enabling a novel route to access hydrodebromination substrates. Further optimization of the reactions still needs to be undertaken and once complete, a detailed mechanistic understanding can be developed (i.e. with deuterium labelled studies). In summary, work has been undertaken to develop a metal free, catalytic hydrodebromination reaction.

References:

(1)Mühdorf, B.; Wolf, R. "Photocatalytic benzyl C-H bond oxidation with a flavin scandium complex" Chem. Commun., 2015, 8425

Electrochemical Carbochlorination of Alkenes

Anthony Allen, Oberlin College

Abstract

Although electricity has been used to effect chemical transformations since at least the turn of the 19th century, their use in organic synthesis has been overshadowed, underutilized, and underappreciated.¹ In their efforts to develop new reaction methodologies, synthetic organic chemists have by convention turned to increasingly exotic redox reagents to perform redox transformations. Most textbooks will mention electroorganic reactions such as the Kolbe electrolysis only in passing. While there has been a persistent undercurrent in the synthetic community regarding electroorganic methods since the late 20th century, an upsurge in interest within the latter half of the past decade has proved to be a boon for the discovery of novel and powerful redox reactions.² Herein is detailed the development of an electrochemical carbochlorination reaction of alkenes, specifically the synthesis of several active C–H bond substrates (Figure 1). The highlights of this electrochemical difunctionalization reaction include its mild conditions, formation of a C–C bond, and introduction of several functional groups with well-established synthetic utility.

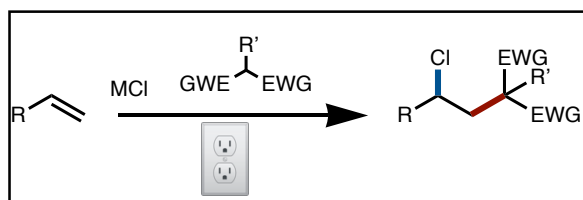


Figure 1 Electrochemical Carbochlorination reaction scheme. The active C–H bond substrates are represented by the di-EWG compound

Introduction

In previously reported works from the Lin lab, electrosynthetic methods were used to homo-difunctionalize alkenes including diazidation and dichlorination reactions.³ Forays into hetero-difunctionalization reactions had also been successful, yielding an aminooxygenation reaction summarized in Figure 2. Although literature precedent exists for such reactions, those systems rely on transition-metal and other redox reagent mediated processes.⁴ In the spirit of the lab's commitment to exploring sustainable, green, and novel reactions, it was decided that modifying these previous electrosynthetic methodologies could accommodate the introduction of a sufficiently electron-

deficient carbon radical specie as one of the difunctionalization adducts. Such a

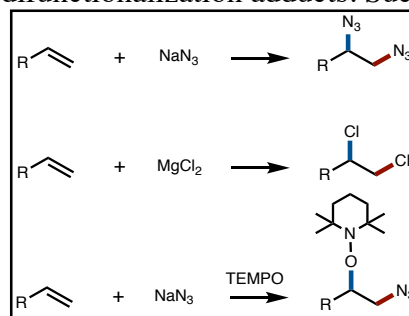


Figure 2 Reaction schemes for previous difunctionalization reactions in the Lin lab. Dichlorination and aminooxygenation papers forthcoming
specie could be generated *in situ* following proton abstraction from active C–H bond compounds

such as geminal dinitriles, β -keto esters, and 1,3-diketo compounds. The electron-withdrawing properties of these functional groups not only increase the reactivity of the C–H bond, but also enhance the electrophilicity of the subsequent carbon radical.

After nucleophilic trapping of this carbon radical by the alkene, a second radical such as chlorine could react with the adduct carbon radical intermediate in order to yield the desired vicinally hetero-difunctionalized product (Figure 3). The addition of this second radical specie is mediated by a radical transfer agent such as the anodically generated $\text{Mn}^{\text{III}}\text{-Cl}$ complex. The manganese in the reaction system is derived from a Mn^{II} catalyst such as those used in the lab's previous difunctionalization reactions. The chloride source is being tested amongst various group I and II salts.

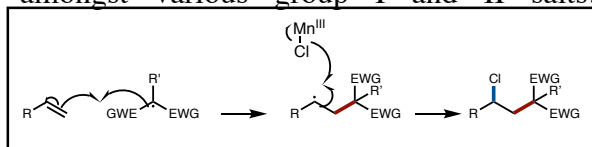


Figure 3 Key bond-forming steps of the carbochlorination reaction

The concomitant formation of a C–C bond, introduction of a chloro group, and installation of two electron-withdrawing groups has excellent synthetic utility. Such a reaction has no literature precedent without the use of stoichiometric quantities of redox reagents. Interesting molecular architectures can be created following further reactions of these difunctionalization products. At the chloro position, substitution reactions can yield hydroxyl compounds which can be further oxidized to the ketone. A bevy of aryl-coupling reactions such as the Heck, Negishi, Sonogashira, and Suzuki could be employed to introduce aromatic moieties into the difunctionalized product. For the electron-withdrawing groups, nitriles can be reduced to primary amines, hydrolyzed to carboxylic acids, converted into ketones

through Grignard reactions, or, after reduction to the amine, cyclize to the chloro position to form substituted pyrrolidines. If the electron-withdrawing groups are keto or ester functional groups, reduction to the alcohol, Grignard reactions, and other nucleophilic addition or acyl substitution reactions are all possible ways to derivatize the difunctionalization product. As with the previous difunctionalization reactions within this lab, it is anticipated that this reaction methodology will tolerate a variety of different substrate functional groups, be scalable, and enable efficient construction of valuable synthetic intermediates in drug, natural product, or pesticide design.

In order to gain mechanistic insight and test the reactive compatibility of this system, a broad substrate scope of active C–H bond compounds was designed and synthesized (Figure 4).

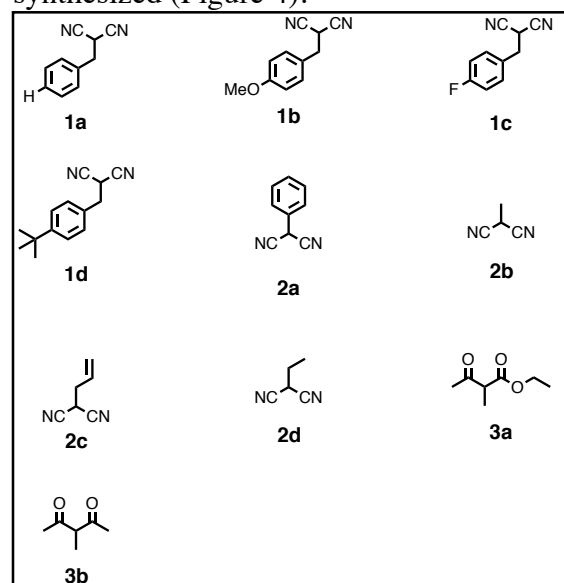


Figure 4 Active C–H bond compound substrate scope

The synthesis of several tetra-substituted alkenes was also attempted (Figure 5). These substrate syntheses were the primary aim of my research experience in the lab and the rest of this report will detail my work in this regard.

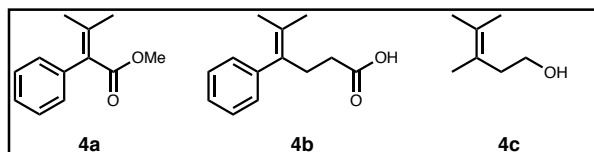


Figure 5 Tetra-substituted alkene substrates

Results and Discussion

Various substituted malonitriles, β -keto esters, and diketo compounds were synthesized over the course of the summer. Compounds **1a-d** were the first class of compounds synthesized. These compounds were synthesized in a two-step process in which a Knoevenagel condensation reaction between malonitrile and the various para-substituted benzaldehydes with 1-methyl imidazole as a catalyst in order to yield the benzylidene malonitrile intermediates. Subsequent borohydride reduction of these intermediates yielded the desired benzyl substituted malonitriles (Figure 6)

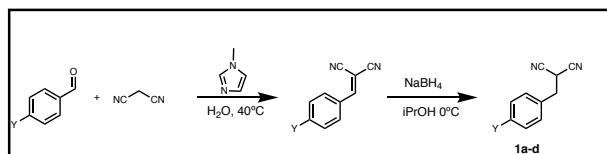


Figure 6 Synthesis of benzyl substituted malonitriles. **1a**, Y = H. **1b**, Y = OMe. **1c**, Y = F. **1d**, Y = t-Bu

The next class of compounds **2a-d** were synthesized by different substitution reactions. Compound **2a** was synthesized through a nucleophilic aromatic substitution reaction between malonitrile and iodobenzene utilizing potassium carbonate as the base to generate the nucleophile malonitrile anion and CuI and L-proline as catalysts (Figure 7).⁵

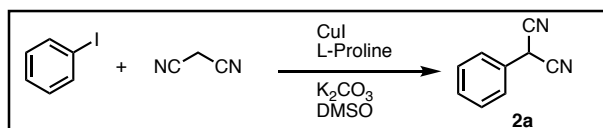


Figure 7 Synthesis of phenylmalonitrile

Compounds **2b** and **2c** were synthesized using two different methods.^{6,7} In the first, malonitrile was reacted with alkyl halide in the presence of potassium carbonate and 4

mol % *tert*-butyl ammonium bromide as a phase transfer catalyst to yield the desired substituted malonitrile. No solvent was used for this substitution reaction. Compound **2d** was also synthesized according to this method. The second method for the synthesis of **2b** and **2c** utilized diisopropylethylamine as base in dichloroethane as the solvent (Figure 8).

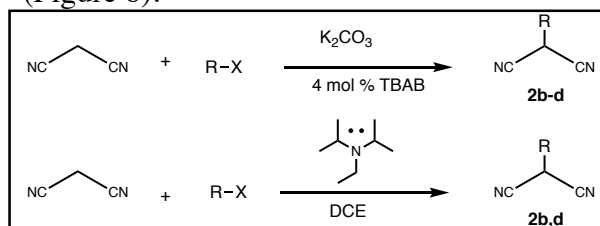


Figure 8 Synthesis of alkyl substituted malonitriles **2b-d**. **2b**, R = Me. **2c**, R = Allyl. **2d**, R = Et

Compound **3a** was synthesized by reacting ethyl-3-oxobutanoate with methyl iodide in the presence of potassium carbonate (Figure 9).⁸

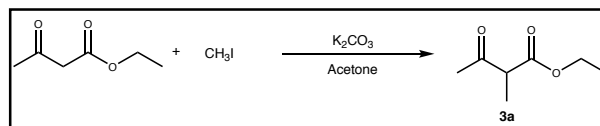


Figure 9 Synthesis of methyl-substituted β -keto ester **3a**

Compound **3b** could have been similarly synthesized with acetyl acetone as the substrate, but as **3b** is commercially available and in the inventory of the lab, I was not needed to synthesize it. All reactions except **1a-d** were performed under a N_2 atmosphere. Please see the experimental section of this report for further detailed information about the procedure, scale, and yields of these reactions.

Turning our attention to the other reactant in the carbochlorination reaction, I was also tasked with the synthesis of several alkenes **4a-c** (Figure 5). Each tetra-substituted alkene contained functional groups such as an ester, carboxylic acid, and hydroxyl in order to test if the carbochlorination reaction could tolerate

these groups. My attempts at the synthesis of these three alkenes all employed the Wittig reaction. Compounds **4a,b** were synthesized by reaction of the respective substrates with isopropyltriphenylphosphorane ylide generated *in situ* through reaction of isopropyltriphenylphosphonium iodide salt with potassium carbonate in THF (Figure 10).

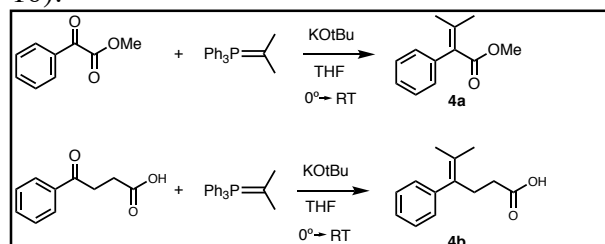


Figure 10 Synthesis of tetra-substituted alkenes **4a,b**.

Alkene **4a** was unable to be isolated. ¹H NMR spectroscopy of the product mixture following column chromatography indicated that **4a** was indeed the major product in the reaction. Further column chromatography and distillations could not yield a fully pure product. The reaction for synthesis of **4b** failed. NMR spectroscopy of the crude reaction mixture following workup revealed that only starting material remained. The presence of the carboxylic acid moiety in **4b** could interfere with the basic conditions of the Wittig reaction. Alkene **4c** required a multi-step synthesis due to the presence of its hydroxyl group. The first step in this synthesis was protection of the hydroxyl group as a silyl ether with the use of *tert*-butyldimethylsilyl chloride and imidazole as a catalyst. The silyl ether could then be safely reacted in the same manner as substrates **4a, b** to yield a tetra-substituted alkenyl silyl ether intermediate. Deprotection of the silyl ether group would then yield the desired tetra-substituted alkene **4c** (Figure 11).

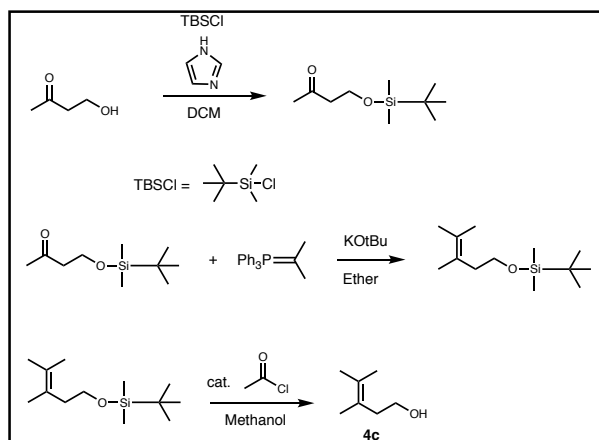


Figure 11 Multistep synthesis of tetra-substituted alkene **4c**

While the protection reaction produced the silyl ether in good yield, the key Wittig reaction in the next step did not. ¹H NMR of the crude product mixture following work up did not show any signs of the desired alkenyl silyl ether product. In the cases of these Wittig reactions, I believe the use of a stronger base such as *n*-Butyl lithium rather than potassium *tert*-butoxide would have yielded better results. If I had more time during the summer, I would focus my attention on rerunning these reactions with *n*-Butyl lithium. All these reactions were performed under a N₂ atmosphere. Please refer to the experimental section of this report for detailed information about the procedure and scale of these reactions.

At the time of this report, the electrochemical carbochlorination reaction is still being optimized by my mentor Dr. Niankai Fu. While better results have since been obtained, I am only able to share his initial results with you at this time (Figure 12). Benzylmalonitrile is the model substrate for the reaction. For more information on this project, a paper should be forthcoming within the next year completely detailing the reaction, its scope, and its mechanism.

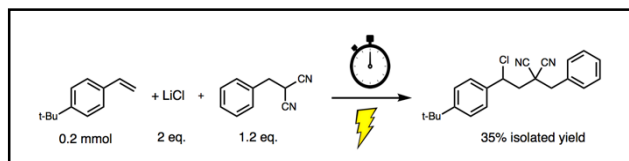


Figure 12 Initial carbochlorination results obtained by Dr. Niankai Fu of the Lin lab.

Conclusion

Even in the incipient stages of its coming-of-age, electroorganic synthesis has breathed a breath of fresh air into organic chemistry. The use of electricity to perform organic redox chemistry in lieu of deleterious and expensive redox reagents is as synthetically innovative as it is environmentally beneficial; we are in the midst of a methodological renaissance whose novelty has the ability to redefine conventional approaches to synthesis. The utility, popularity, and adoption of electroorganic methodology is undeniably growing as each new edition of the field's top peer-reviewed journals feature articles implementing electrosynthesis.

The Lin lab is on the cutting-edge of this movement as it continues to develop difunctionalization reactions such as the carbochlorination reaction described herein. My small part in working on this project during summer through substrate synthesis was immensely rewarding in both its successes and failures. The substrates that I synthesized will be used to gain valuable information about the reaction's mechanism and scope. I hope – for both the health of the world and organic chemistry community – that continued research in electroorganic synthesis yields powerful results in natural product synthesis, drug design, and industrial chemical processes.

Acknowledgments

I am grateful first and foremost for the support, direction, and guidance of my brilliant mentor Dr. Niankai Fu. I would also like to thank Professor Song Lin for allowing me to conduct research in his lab this summer and for his advice throughout this experience. I am indebted to many of the members of the Song Lin lab including Keith Carpenter, Juno Castillo Siu, Xiangyu Wu, Dr. Keyin Ye, Ambarneil Saha, Dr. Wei Hao, James Sun, and Gregory Sauer for aiding me in my day-to-day laboratory challenges. I would like to thank the CCMR and NSF for providing the funding for this wonderful opportunity to budding scientists. Finally, I would like to thank members from my home institution of

Oberlin College including Dr. Theodore R. Schroeder, Christian Flynn, Matthew Bullock, Andrew Nolan, Federico Consuegra, and Jerome Garcia.

References

1. Horn, E.J.; Rosen, B.R.; Baran, P. S. "Synthetic Organic Electrochemistry: An Enabling and Innately Sustainable Method." *ACS Cent. Sci.*, **2016**, *2*, 302–308
2. Francke, R.; Little, R.D. "Redox Catalysis in Organic Electrosynthesis: Basic Principles and Recent Developments." *Chem. Soc. Rev.*, **2014**, 2492-2518
3. Fu, N.; Sauer, G.; Saha, A.; Loo, A.; Lin, S. "Metal Catalyzed Electrochemical Diazidation of Alkenes" *Science*, **2017**, forthcoming
4. Yuan, Y.-A.; Lu, D.-F.; Chen, Y.-R.; Xu, H.* "Iron-Catalyzed Direct Diazidation for a Broad Range of Olefins" *Angew. Chem. Int. Ed.* **2015**, *55*, 234-238
5. J. Li, M. J. Lear, Y. Hayashi, *Angew. Chem. Int. Ed.* **2016**, *55*, 9060
6. Barra, E.D; Hoz, A.; Moreno, A.; Verdu-Sanchez, P "Phase Transfer Catalysis Without Solvent. Synthesis of cycloalkane-1,1-dicarbonitriles and alkanetetracarbonitriles" *J. Chem. Soc., Perkin Trans. 1*, **1991**, *0*, 2593-2596
7. Ghorai, M.; Talukdar, R. ; Tiwari, D.P "A Route to Highly Functionalized β -Enaminoesters via a Domino Ring-Opening Cyclization/Decarboxylative Tautomerization Sequence of Donor–Acceptor Cyclopropanes with Substituted Malononitriles" *Org. Lett.*, **2014**, *16*, 2204–2207
8. Ravía, S.P.; Carrera, I.; Seoane, G. A.; Vero, S.; Gaménara, D. "Novel Fungi-catalyzed Reduction of α -alkyl- β -keto Esters" *Tetrahedron: Asymmetry* **2009**, *20*, 1393–1397

Experimental

All experiments were carried out in clean, oven-dried glassware with a magnetic stir bar under an N₂ atmosphere unless otherwise noted. TLC was performed on Merck F₂₅₄ silica-gel plates. All NMR spectroscopy was performed on Bruker 300 or 400 MHz NMR spectrometers.

Synthesis of substituted malonitriles 1a-d

Malonitrile (30 mmol) was weighed into a 200 mL round bottom flask. Distilled water (40 mL) was added to the flask before addition 1-methyl-imidazole (80 μ L). Using a pasteur pipette, a pre-weighed portion of the appropriate benzaldehyde (30 mmol) was added to the malonitrile solution. The reaction was run in a 45°C oil bath. The flask was left open to the air and the reaction was monitored by TLC in 4:1 Hexane/Ethyl Acetate solution. Potassium permanganate stains were used to identify the UV inactive malonitrile spots on the TLC. Upon reaction completion, the resulting mixture was vacuum filtered and washed in methanol to yield the benzylidene malonitrile intermediates. All benzylidene intermediates were white powders. From these intermediates, 10 mmol was weighed into a 100 mL round bottom flask. Isopropanol (20-25 mL) was used to dissolve the powders before slow addition of sodium borohydride (15 mmol) to the flask at 0°C. The flask was left open to the air to react at room temperature and the reaction was monitored by TLC in 4:1 Hexane/Ethyl acetate solution. Upon reaction completion, the reaction mixture was slowly quenched with 2M HCl at 0°C. The reaction mixture was extracted with three portions of 25 mL of dichloromethane. The combined organic layers were dried with sodium sulfate and concentrated *in vacuo*. Crude product was purified by flash column chromatography using 9:1 Hexanes/Ethyl acetate solution. All

products were white powders. The purity of each product was confirmed by ^1H NMR.

Yields

1a 60%, **1b** 47%, **1c** 60%, **1d** 33%.

Synthesis of phenylmalonitrile 2a

Malonitrile (30 mmol) was weighed into a 3-neck 250 mL round bottom flask. CuI and L-proline (2 mmol each) were added to round bottom flask. Potassium carbonate (40 mmol) was added to the flask. The flask was outfitted with rubber sept and then evacuated and filled with N_2 three times. DMSO (150 mL) was syringed into the flask and the solution was allowed to stir for 10 minutes before dropwise addition of iodobenzene (10 mmol). The flask was outfitted with an N_2 balloon and placed in a 95°C oil bath. The reaction was allowed to stir for 36 hours. TLC was performed on the reaction mixture in 3:1 Hexanes/Ethyl acetate solution. Potassium permanganate stain was used to reveal UV inactive malonitrile on the TLC plates. The reaction mixture was loaded onto a 100g Biotage column and chromatography was performed on a 19:1 to 9:1 Hexanes/Ethyl acetate gradient. Purity of subsequent clear, viscous liquid was confirmed by ^1H NMR.

Yield 49%

Synthesis of substituted malonitriles 2b-d

Malonitrile (25 mmol) was weighed into a 50 mL 3-neck round bottom flask. 4 mol% (0.322 g) of *tert*-Butyl ammonium bromide salt was weighed into the flask. The flask was evacuated and filled with N_2 three times. The appropriate alkyl halide (12.5 mmol) was syringed into the flask and left to stir for 30 minutes. The flask was outfitted with an N_2 balloon. Potassium *tert*-Butoxide (**2b**) or potassium carbonate (**2c, d**) (12.5 mmol) was quickly added in one portion to the flask. The reaction was left stir neat for 15 minutes. A thick orange paste formed. The reaction mixture was extracted in three portions

totaling 200 mL of dichloromethane. The combined organic layers were dried over sodium sulfate and concentrated *in vacuo*. Flash column chromatography with 9:1 Hexanes/Ethyl acetate solution was used to yield substituted malonitriles **2b-d**. The purity of these compounds was confirmed by ^1H NMR. An unexpected singlet at 2.3 ppm was present in each of these compounds.

Yields

2b 29% **2c** 56% **2d** 37%

Synthesis of substituted malonitriles 2b,c

Method 2

Malonitrile (9 mmol) was weighed into a 3-neck 100 mL round bottom flask outfitted with three rubber septa. The flask was evacuated and filled with N_2 three times. Dichloroethane (18 mL) was syringed into the flask and the solution was allowed to stir for 5 minutes. *N,N*-diisopropylethylamine (9 mmol) was added dropwise into the flask at 0°C followed by dropwise addition of the appropriate alkyl halide also at 0°C . The flask was outfitted with an N_2 balloon. The reaction was left to react at room temperature and monitored by TLC in 9:1 Hexanes/Ethyl acetate solution. Potassium permanganate stain was used to reveal UV inactive malonitrile spots. Upon reaction completion, the reaction was quenched with addition of distilled water (18 mL). The reaction mixture was extracted three times with 40 mL of ethyl acetate. The combined organic layers were washed with brine, dried over sodium sulfate, and concentrated *in vacuo*. Flash column chromatography ran at 300 mL 19:1 Hexanes/Ethyl acetate followed by 9:1 Hexanes/Ethyl acetate solution yielded the desired substituted malonitriles. The purity of these compounds was confirmed by ^1H NMR

Yields

2b 17% **2c** 39%

Synthesis of ethyl 2-methyl-3-oxobutanoate 3a

Ethyl-3-oxobutanoate (31 mmol) was weighed into a 3-neck 100 mL round bottom flask outfitted with two rubber septa and a reflux condenser. The system was evacuated and filled with N₂ three times. Acetone (40 mL) was syringed into the flask. Potassium carbonate was quickly added in one portion and the reaction was stirred vigorously for 10 minutes. Methyl iodide (38 mmol) was syringed into the flask and the reaction was left to reflux at 65°C. The reaction was monitored by TLC in 9:1 Hexanes/Ethyl acetate solution. Upon completion, the reaction was allowed to cool to room temperature before diethyl ether (60 mL) was added to the flask. The resulting mixture was filtered and the filtrate was concentrated *in vacuo*. The resulting viscous liquid was loaded onto a 100 g Biotage column and ran at a 95% Hexane/Ethyl acetate to 85% Hexane/Ethyl acetate gradient to yield **3a**. The purity of the compound was confirmed by ¹H NMR.

Yield 42%

Synthesis of tetra-substituted alkene 4a

Isopropyltriphenylphosphonium iodide (10 mmol) was weighed into a 3-neck 100 mL round bottom flask outfitted with 3 rubber septa. The flask was evacuated and filled with N₂ three times. Anhydrous THF (50 mL) was syringed into the round bottom flask at 0°C. The solution was allowed to stir for 5 minutes before quick addition of potassium tert-Butoxide (10 mmol) in one portion at 0°C. The mixture was left to stir for 30 minutes in order to generate the desired isopropyltriphenylphosphorane ylide.

Methyl-2-oxo-2-phenylacetate (5 mmol) was then added dropwise to the solution at 0°C. The reaction was monitored by TLC in 9:1 Hexanes/Ethyl acetate solution. Upon reaction completion, the reaction mixture was diluted with hexanes to precipitate the phosphonium oxide. The reaction mixture was filtrated and the filtrate was concentrated

in vacuo. Flash column chromatography was unable to separate the desired product from an unknown contaminant following two columns at 95% Hexanes/Ethyl acetate and then 100% Hexanes solution. ¹H NMR of the product mixture indicated that the desired **4a** was the major product. Further attempts at distillation of the product mixture at 90°C had mixed success.

Synthesis of tetra-substituted alkene 4b

Isopropyltriphenylphosphonium iodide (6 mmol) was weighed into a 3-neck 100 mL round bottom flask outfitted with 3 rubber septa. The flask was evacuated and filled with N₂ three times. Anhydrous THF (12 mL) was syringed into the round bottom flask at 0°C. The solution was allowed to stir for 5 minutes before quick addition of potassium tert-Butoxide (10 mmol) in one portion at 0°C. The mixture was left to stir for 30 minutes in order to generate the desired isopropyltriphenylphosphorane ylide. 4-oxo-4-phenylbutanoic acid (5 mmol) was then added dropwise to the solution at 0°C. The reaction was monitored by TLC in 9:1 Hexanes/Ethyl acetate solution. Upon reaction completion, the reaction mixture was concentrated *in vacuo*. Dichloromethane (50 mL) and 1M NaOH (50 mL) were used to dilute the concentrate. The aqueous layer was acidified to ~ pH 2 with 12 M HCl. The aqueous layer was extracted three times with 30 mL dichloromethane. The combined organic layers were dried over sodium sulfate and concentrated *in vacuo*. A crude NMR revealed that all that remained was starting material.

Synthesis of tetra-substituted alkene 4c

4-hydroxy-2-butanone (20 mmol) and imidazole (30 mmol) were weighed into a 200 mL round bottom flask. The flask was evacuated and filled with N₂ three times.

Dichloromethane (50 mL) was added to the flask. *Tert*-butyldimethylsilyl chloride (22 mmol) was quickly added in one portion to the flask and the reaction was left to stir overnight. The flask was outfitted with an N₂ balloon. A TLC was performed in 9:1 Hexanes/Ethyl acetate solution. The reaction mixture was concentrated *in vacuo*. The concentrate was purified through flash column chromatography with in 9:1 Hexanes/Ethyl acetate solution to yield the keto silyl ether intermediate.

Isopropyltriphenylphosphonium iodide (3.6 mmol) was weighed into a 3-neck 100 mL round bottom flask outfitted with 3 rubber septa. The flask was evacuated and filled with N₂ three times. Anhydrous diethyl ether (20 mL) was syringed into the round bottom flask at 0°C. The solution was allowed to stir for 5 minutes before quick addition of potassium *tert*-Butoxide (3.6 mmol) in one portion at 0°C. The mixture was left to stir for 30 minutes in order to generate the desired isopropyltriphenylphosphorane ylide. The keto silyl ether from the previous reaction (3 mmol) was then added dropwise to the solution at 0°C. The reaction was left to run overnight. A TLC was performed in 9:1 Hexanes/Ethyl acetate solution. The reaction mixture was diluted with hexanes to precipitate the phosphonium oxide. The reaction mixture was filtrated and the filtrate

was concentrated *in vacuo*. A crude NMR revealed that no desired product had formed.

Carbon Supported Pd-Mn Alloy Catalysts for Oxygen Reduction Reactions in Alkaline Fuel Cells

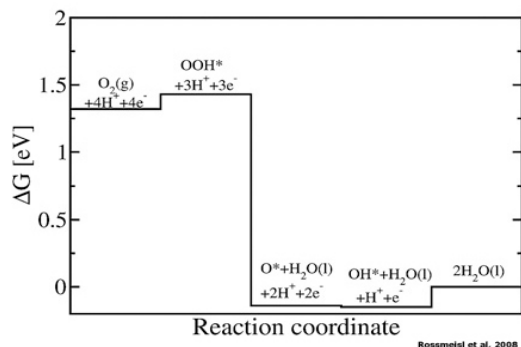
By: Omar Alqahtani

Abstract—For the purposes of finding an alternative to Platinum as a catalyst for fuel cells, this paper investigates Pd-Mn alloy as an electrocatalyst to Oxygen Reduction Reactions(ORR). After the successful synthesis of Pd₇Mn₃/C and evaluating the ORR activities in alkaline media and comparing them to that of Pd/C it was determined that it was concluded that Mn harmfully affects the Pd ORR activity.

Index Terms—ORR, Palladium, Fuel cells, Pd-Mn Alloy, electrocatalyst

I. Introduction

Fuel cells are an energy conversion technology much like batteries. However, unlike batteries they do not require recharging if the supply of fuel is constant. One type of fuel cells rely on Oxygen Reduction Reactions (ORR), which are a branch of oxygen electrode reactions. Although the oxygen electrocatalytic reactions are one of the most studied topics in electrochemistry, the mechanism of ORR is still not well understood. The most accepted mechanism involves 4 steps with two rate determining steps(RDM) which are dictated by the adsorption affinity of the catalyst's surface.



I. Rossmeißl et al., 2008

The two RDMs have contrasting effects if the oxygen adsorption is too weak the reaction does not start, and if it is too strong the surface the oxygen does not leave the surface and it covers the active sites of the catalyst preventing any further reactions. This is correlated to the metal d-band center in the figure below.

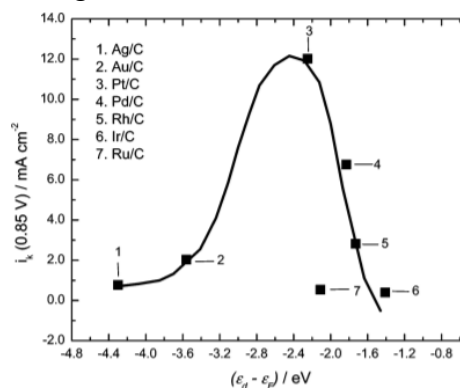


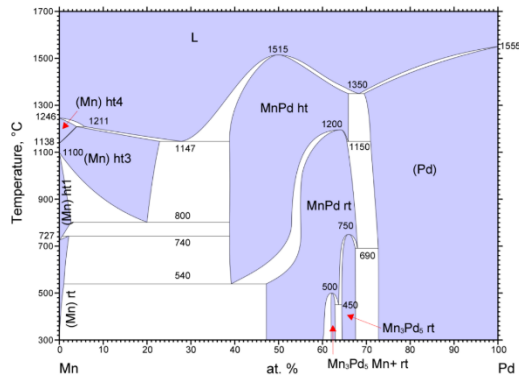
Figure 8. Kinetic currents (i_k) at 0.80 V vs RHE for the O_2 reduction on carbon-supported metal nanoparticles in 0.1 mol L^{-1} NaOH solution as functions of the metal d-band center ($\epsilon_d - \epsilon_F$; relative to the Fermi level).

2. Lima et al. 2007

The volcano plot shows the optimization nature with Platinum achieving the optimal d-band center for the best ORR activities in alkaline media and so far, it has been the common choice for a catalyst in fuel cells. Nonetheless, Platinum is very expensive and is not economically feasible with large scale production needed for applications like transportation. One way to solve this problem is to investigate palladium-based alloys as an alternative to platinum. Since palladium has comparable activities to platinum at almost half the cost, and alloying palladium with smaller elements should improve the mass specific activity or not affect it enough to make the catalyst more economically

II. Procedure

Before starting the synthesis, we refer to the alloy phase diagram of Pd-Mn to know the ratios and temperatures we can use to achieve a single-phase diagram (in blue).



3. Phase diagram from ASM Alloy Phase database

As the diagram shows there is not a lot of freedom when it comes to choosing the Pd to Mn ratio. A ratio of (1:1) was chosen, but first Pd Nanoparticles were synthesized to be used later to compare Pd-Mn particles to.

1. Carbon supported Palladium NP synthesis:

$\text{Pd}(\text{NO}_3)_2 \cdot 2\text{H}_2\text{O}$ was used as the precursor, dissolved in THF with carbon (20% metal loading) and sonicated with a probe sonicator while magnetically stirring for 30 minutes. Then an excessive amount of the reducing agent, NaBH_4 , was added to the solution dropwise while stirring and sonicating in an ice bath and left sonicating for another 30 minutes. The NP were later collected and the NaBH_4 was rinsed off the sample with DI water. After that the dry NP were Annealed at 200°C for two hours in forming gas (95% N_2 , 5% H_2).

2. Carbon Supported Palladium Manganese alloy NP synthesis:

Synthesizing Pd-Mn alloy was a difficult task largely because Manganese, with a reducing potential of -1.18V , was very

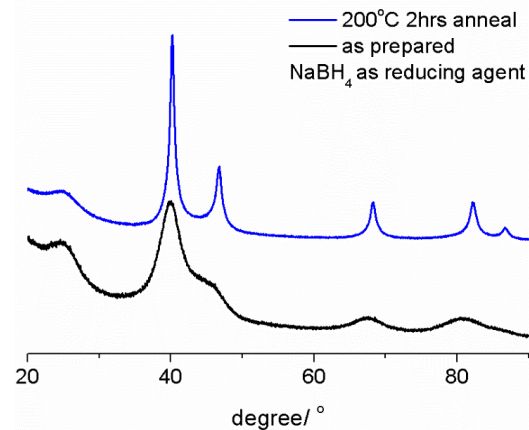
difficult to reduce. So, after going through several different methods the following method gave us the best results.

$\text{Pd}(\text{acac})_2$ and $\text{Mn}(\text{acac})_2$ were used as the precursors, dissolved in triethylene glycol after sonicating for 15 minutes Vulcan carbon 72R was added as support, With 20% metal loading and the solution as sonicated for another 30 minutes. The reaction was carried at 230°C in a silicon oil bath for one hour under Nitrogen atmosphere while stirring. The solution was washed with ethanol/acetone three times then with NaOH /ethanol solution three times as well to remove the surfactant, and collected with centrifuge and then vacuum collected.

III. Results & Discussion

1. Pd/C characterization

After synthesizing the nanoparticles X-Ray diffraction was used to characterize the crystal structure of the NPs.

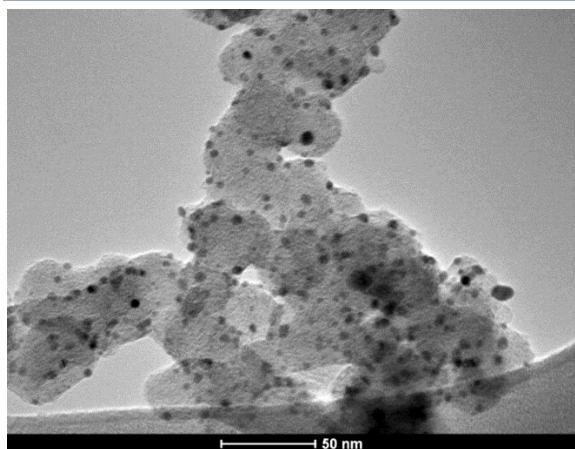


4. X-ray diffraction pattern of synthesized Pd/C NPs

The XRD of Pd/C NPs follows the pattern of Pd from the ICSD data base. The size of the particles was then estimated using the Scherer equation:

$$\tau = \frac{K\lambda}{\beta \cos \theta}$$

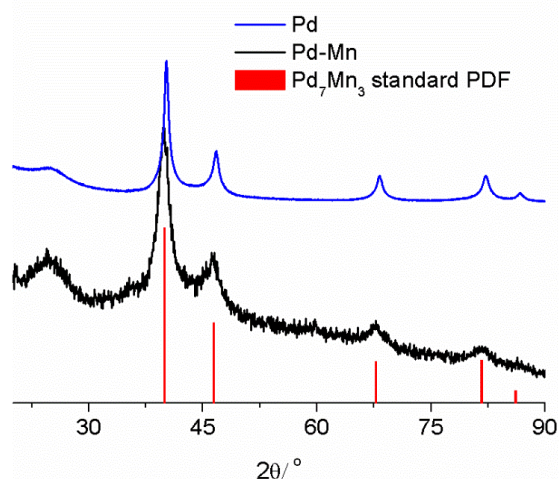
The particles' size is approximately 7.0nm which is within the appropriate size limit. It should be noted that the particle size was calculated after annealing for two hour. The sample was annealed because from the XRD pattern, some of the Pd NPs were still amorphous. After annealing sharper peaks were obtained with XRD.



5 TEM image of synthesized Pd/C before annealing

TEM images of the Pd/C sample shows good distribution of NPs on the carbon support for the best which would maximize the Pd active surface area, and the ORR activity.

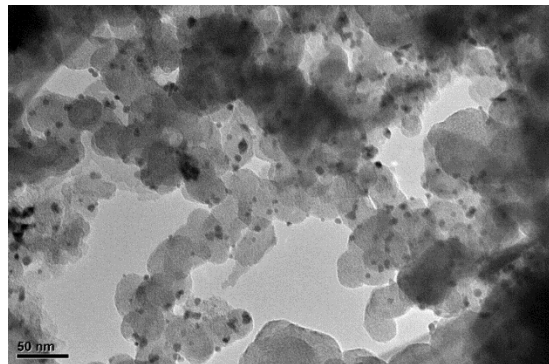
2. Pd-Mn/C NPs characterization



6 XRD trend of Pd-Mn/C compared with that of Pd/C and the peak positions of Pd₇Mn₃ from the data base

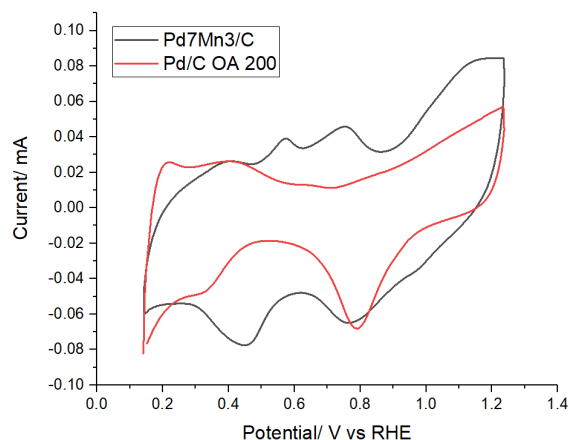
XRD pattern of Pd-Mn has a lower quality than that of the Pd, because a different instrument was used. However, the pattern has enough

quality to determine the shape and lattice parameter of the sample. After comparing with the data base, it was found that the sample pattern was the same as Pd₇Mn₃ which is not the ratio meant to be synthesized, most likely it was difficult to all the Mn. Nevertheless, this new ratio is still a single-phase alloy so, it was decided that it would be tested.



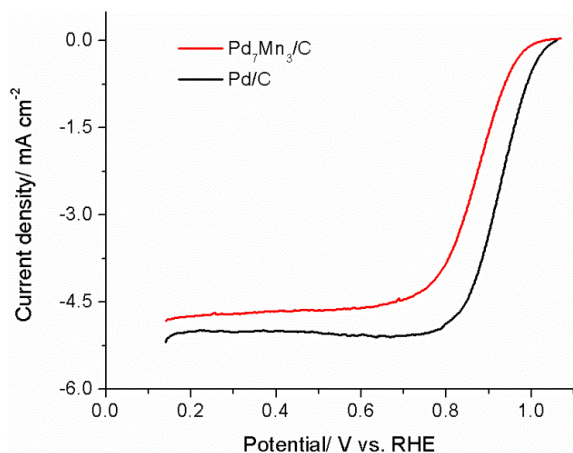
7 TEM Image of Pd-Mn unannealed

TEM image shows good distribution on the carbon support.



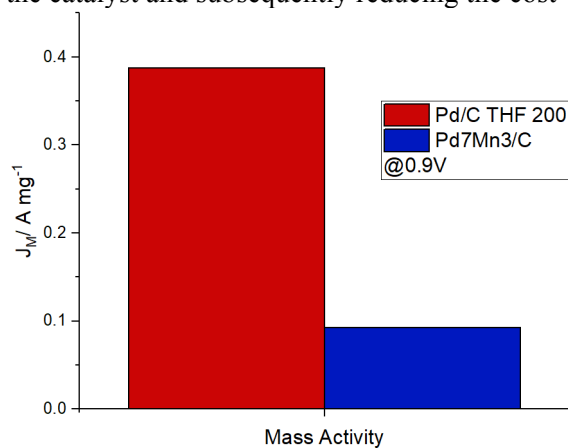
8 Cyclic-Voltammogram of both samples in 0.1M NaOH at 50mV/s

After depositing the samples on the electrodes and running several cycles to clean the surface the CV of both samples was taken in 0.1M NaOH media, and by comparing them above we notice extra peaks on the Pd-Mn CV because of the presence of Mn in the sample.



9 ORR activity. 1600RPM @5mV/s

The difference in ORR activity between Pd/C and Pd₇Mn₃/C can be compared by the half-wave potential. Pd₇Mn₃/C half-wave potential is approximately 60mV less than Pd/C which is bad but the final verdict on Pd₇Mn₃/C as a catalyst for ORR depends on the mass activity. If the mass activity is comparable to Pd/C, then Pd₇Mn₃/C can reduce the amount of Pd used in the catalyst and subsequently reducing the cost



From the palladium mass activity comparison it can be concluded that the addition of Mn to Pd harmfully affect the activity of palladium, most likely by covering the active sites of Palladium.

IV. Conclusion

After the successful synthesis of carbon supported Pd & Pd₇Mn₃, X-ray diffraction and TEM were used to characterize and evaluate the synthesis of the nanoparticles. Electrochemical measurements such as cyclic voltammetry and Rotating Disk Electrode (RDE) were taken to evaluate the ORR activity of both samples. After

Analyzing the obtained data on Pd and Pd₇Mn₃ nanoparticles ORR activity in alkaline media it was concluded that Mn harmfully affects the Pd ORR activity.

V. Acknowledgment

I would like to thank Prof. Abruña, Prof. DiSalvo, Yin Xiong, Yao Yang and all other members of the Abruña group for all the help and support they gave me while working on this project, and for providing me a welcoming and friendly environment that helped my learning of the subject.

References:

Rossmeisl, Jan, et al. "Steady state oxygen reduction and cyclic voltammetry." *Faraday discussions* 140 (2009): 337-346.

Lima, F. H. B., et al. "Catalytic Activity– d-Band Center Correlation for the O₂ Reduction Reaction on Platinum in Alkaline Solutions." *The Journal of Physical Chemistry C* 111.1 (2007): 404-410.

Ge, Xiaoming, et al. "Oxygen reduction in alkaline media: from mechanisms to recent advances of catalysts." *ACS Catalysis* 5.8 (2015): 4643-4667.